Project 074 Low Emissions Pre-Mixed Combustion Technology for Supersonic Civil Transport

Georgia Institute of Technology

Project Lead Investigator

Adam Steinberg
Associate Professor
School of Aerospace Engineering
Georgia Institute of Technology
620 Cherry Street
Atlanta, GA 30313
404-897-1130
adam.steinberg@gatech.edu

University Participants

Georgia Institute of Technology (GT)

- P.I.: Adam Steinberg, Associate Professor, School of Aerospace Engineering
- FAA Award Number: 13-C-AJFE-GIT-079
- Period of Performance: August 11, 2020 to September 30, 2023
  Period of Performance Covered in Report: October 1, 2021 to September 30, 2022
- Tasks:
  1. Experimental measurement of flame structure, combustion dynamics, and emissions
  2. Large eddy simulations of combustor operation and emissions
  3. Thermoacoustic modeling

Project Funding Level

FAA: $1,999,998
GT: $1,000,262
GE Research: $999,736

Investigation Team

Name	Affiliation	Role	Tasks
Adam Steinberg Associate Professor	GT	P.I.	Management, reporting, technical oversight of all tasks, oversight of optical diagnostics in Task 1
Ellen Mazumdar Assistant Professor	GT	Co-P.I.	Oversight of OH planar laser-induced fluorescence (PLIF) measurements in Task 1
Joseph Oefelein Professor	GT	Co-P.I.	Oversight of first-principles large eddy simulations (LESs) in Task 2 and overall coordination of Task 2
Jerry Seitzman Professor	GT	Co-P.I.	Oversight of gas-phase fuel/air mixing diagnostics in Task 1
Michael Benjamin Consulting Engineer	GE Aviation	Co-P.I.	Oversight of combustor design in Task 1, coordination of GT/GE LES collaboration in Task 2

Krishna Venkatesan **Principal Engineer**	GE Research	Co-P.I.	Oversight of combustor operation in Task 1 and data collection for Task 3
Oleksandr Bibik **Senior Research Scientist**	GT	Participant	Task 1
Hannah Bower **Research Engineer**	GE Research	Participant	Task 1
Fei Han **Engineering Manager**	GE Research	Participant	Task 3
John Hong **Lead Engineer**	GE Research	Participant	Task 1
Nick Magina	GE Research	Participant	Task 3
Victor Salazar **Lead Engineer**	GE Research	Participant	Task 1
R. Narasimha Chiranthan	GE Aviation	Participant	Task 2
Manampathy Giridharan	GE Aviation	Participant	Task 2
Hiranya Nath	GE Aviation	Participant	Task 2
Sriram Kalathoor **Graduate Research Assistant**	GT	Graduate Student	Task 2
Mitchell Passarelli **Graduate Research Assistant**	GT	Graduate Student	Task 1 & 3
Sundar Ram Manikandan **Graduate Research Assistant**	GT	Graduate Student	Task 1
Samuel Wonfor **Graduate Research Assistant**	GT	Graduate Student	Task 1 & 3
Andrew Zheng **Graduate Research Assistant**	GT	Graduate Student	Task 1
Neilay Amin **Research Assistant**	GT	Undergraduate Student	Task 2
Preethi Mysore **Research Assistant**	GT	Undergraduate Student	Task 2
Coleman Pethel **Research Assistant**	GT	Undergraduate Student	Task 1
Katrina Potak **Research Assistant**	GT	Undergraduate Student	Task 2
Mihir Rao **Research Assistant**	GT	Undergraduate Student	Task 1
Andrew Semelka **Research Assistant**	GT	Undergraduate Student	Task 1
Rachel Wilder **Research Assistant**	GT	Undergraduate Student	Task 2

Project Overview

Market demand for high-speed transport is expected to drive a rapid re-emergence of commercial supersonic transport (CST) aircraft over the coming decades. This impending CST revival, combined with the increasingly harmful impacts of anthropogenic climate change, mandates advancements in CST-focused environmentally compatible technologies and policies. In comparison to subsonic aircraft, engines for CST aircraft (a) operate at a significantly lower overall pressure ratio (OPR) and bypass ratio, (b) experience higher combustor inflow temperatures (T_3), lower pressures (p_3), and higher fuel/air ratios under cruising conditions, and (c) cruise at higher altitudes. The reduced OPR and bypass ratio result in increased thrust-specific fuel consumption, thus increasing fuel burn and making it fundamentally more challenging to reduce emissions. Furthermore, the combination of low OPR and high cruise T_3 and fuel/air ratio (FAR) results in complicated trade-offs between nitrous oxide (NO_x) under cruise conditions and other emissions (CO, nonvolatile particulate matter [nvPM] and unburnt hydrocarbon) at lower power.

Several recent studies have assessed potential CST fleet emissions and environmental impacts based on currently deployed rich burn–quench–lean burn combustors (typically Tech Insertion combustors) designed for subsonic transport (Berton, 2020; Speth, 2021; Hassan, 2020; Kharina, 2018). These studies demonstrate that innovations in combustor architecture will be required to meet emission and efficiency targets, helping to enable an environmentally compatible CST market. Despite the high T_3 and FAR, peak flame temperatures must be moderated to meet NO_x targets, while also maintaining efficiency and achieving low levels of CO, unburnt hydrocarbon, and nvPM. This will require increased fuel-lean pre-mixing prior to combustion.

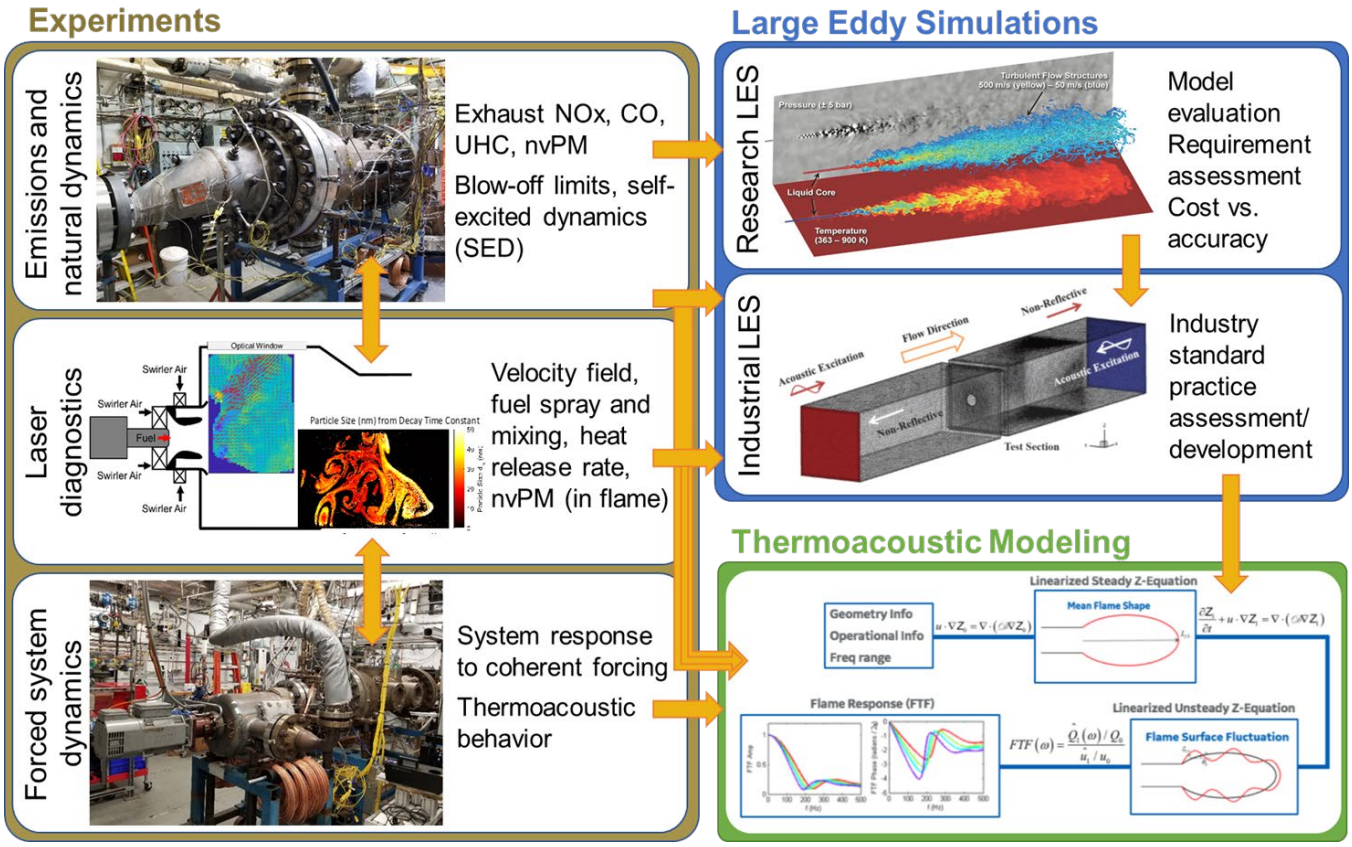

Figure 1. Project overview. FTF: flame transfer function; LES: large eddy simulation; nvPM: nonvolatile particulate matter; UHC: unburnt hydrocarbon.

Lean pre-mixed pre-vaporized (LPP) combustors are a promising path to lowering emissions from future CST engines. In LPP combustors, fuel is injected, partially pre-vaporized, and partially pre-mixed with air before the reactants enter the combustor. While the LPP concept is not new, e.g. (Niedzwiecki, 1992) achieving good vaporization and mixing in a flight-appropriate package has been challenging in the past. However, these issues can potentially be alleviated by the high T_3 in CST combustors—which results in faster vaporization—and advanced manufacturing to enable compact rapid-mixing flow elements.

Thus far, the ability of current design methodologies to predict the operability and emissions of LPP combustors under relevant conditions is unproven. Hence, there is a critical need to generate high-quality experimental data for CST combustor conditions, coupled with the development and validation of computational fluid dynamics (CFD) simulations and reduced-order thermoacoustic models. This project addresses this need through a combination of experiments, LESs, and thermoacoustic modeling, all applied in a novel LPP combustor of interest to future CST applications. Figure 1 shows the elements of this research project.

Task 1 - Experimental Measurements of Flame Structure, Combustion Dynamics, and Emissions

Georgia Institute of Technology

Objective

This task represents the experimental effort to measure the flame structure, dynamics, and emissions in a novel LPP combustor concept, designed specifically for low-emission operation under typical conditions encountered by CST engines.

Research Approach

Efforts under Task 1 over the reporting period consisted of four main activities.

1) Design, fabrication, and deployment of a new LPP combustor test article for experiments in a test cell at GE Research that is capable of acoustic forcing
2) Design, calibration, and deployment of the measurement systems
3) Experimental Campaign 2 to study the forced and self-excited dynamics of the LPP combustor using optical diagnostics from GT that were transported to GE Research and deployed in the GE test cell
    a. GT students were onsite at GE Research for a total of nearly 9 person-months over Summer 2022 to conduct this experimental campaign in collaboration with GE staff.
4) Analysis of the experimental data from Campaigns 1 and 2

Experimental Design, Fabrication, and Deployment

Considerable preliminary work was performed to enable on-schedule execution of Experimental Campaign 2. The following major elements of the test rig at GE Research were designed and fabricated:

1) Test rig spool pieces
2) Optical combustor liner
3) Water-cooled exhaust system with ports for various pressure and emission probes
4) Window blank with pressure measurement ports

Experimental Campaign 2 was undertaken at GE Research between July and September 2022 in the GEB test facility (Figure 2). The THOR rig housed at GEB contains the ASCENT test article and can handle combustion experiments for single-cup fuel nozzle configurations. Figure 3 shows details of the THOR rig vessel assembly. The THOR rig consists of an optically accessible vessel that is rated to 17.2 bar (275 psia) and 810 K (1000 ˚F), which contains several large ports that enable optical and laser access to the test section.

The test article built for Experimental Campaign 2 is shown in Figure 4. The combustor test article consists of an LPP dome, square optical liner, and constant-area tail pipe section. A constant-area hot section was chosen to eliminate any combustor back-projection uncertainties of the acoustic pressure from the downstream multi-microphones. The test article design was based on GE's existing THOR optical liner design, which was successfully employed over the last eight years for various optical and laser diagnostic efforts for aero-engine studies. The LPP dome is shown schematically in Figure 5, consisting of four bluff-body-stabilized pre-mixed flames surrounding a non-pre-mixed swirling pilot; details of the four pre-mixed flames are redacted.

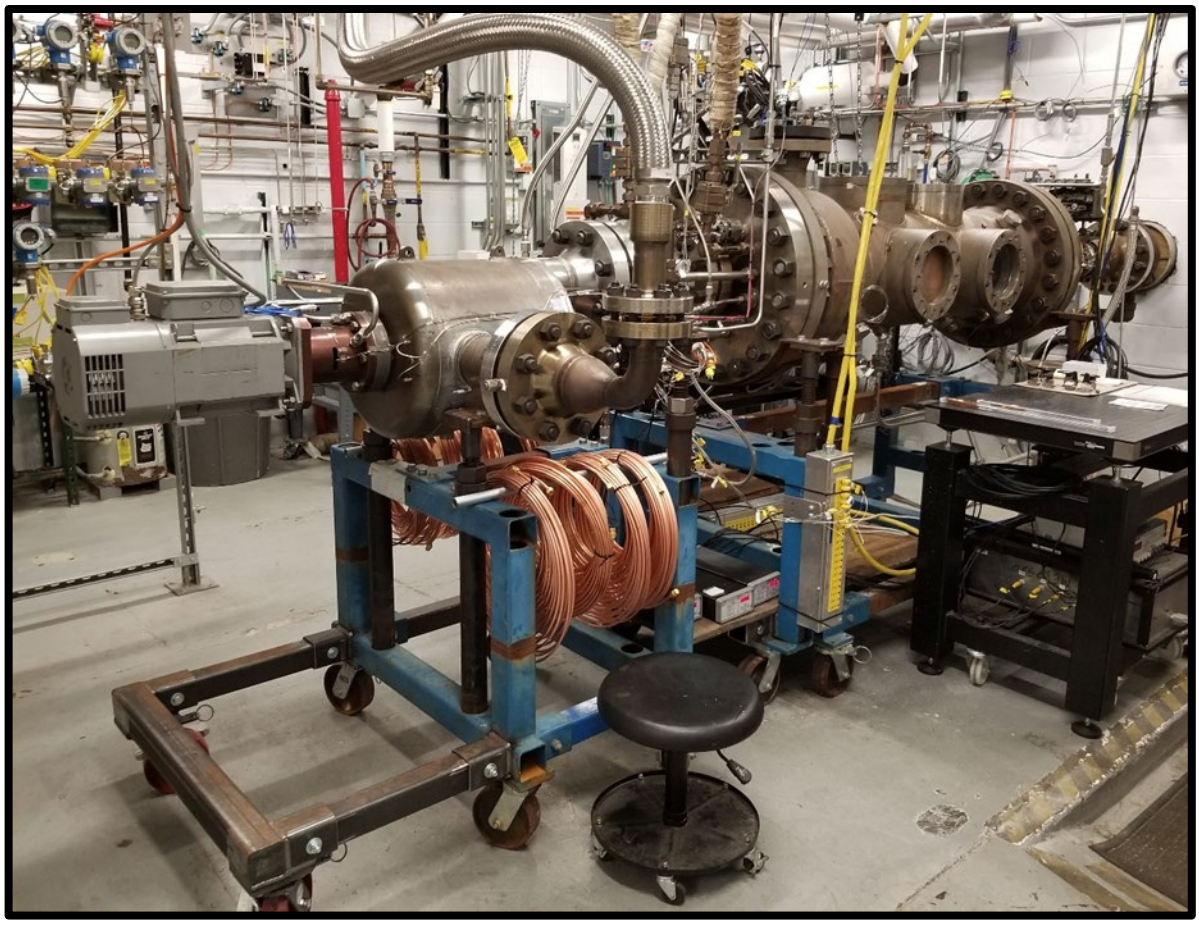

Figure 2. THOR test rig and diagnostic setup at the GEB test facility.

For the various diagnostic measurements employed in this campaign, quartz windows were employed for the side walls and the top wall of the combustor section. The combustor bottom wall was a water-cooled window-blank with ports for an ignitor and three dynamic pressure sensors. The downstream tail pipe consisted of a water-cooled constant cross-section liner with ports for dynamic pressure sensors. A water-cooled orifice plate, located at the end of the tail pipe section, provided the necessary acoustic boundary condition to suppress self-excited combustor tones. The dimensions of this orifice plate were based on the predicted rig tones and designed to withstand thermal loading.

The rig is continuously supplied with high-pressure preheated air for combustor and cooling needs. The typical combustor air flow ranges from 0.2 to 0.4 kg/s, and vessel cooling bypass air is provided at approximately 0.4 kg/s at 600 K. The test facility also features a topping heater that can potentially increase the air temperature delivered to the rig. Three liquid Jet A lines supply fuel to the combustor. One of the three fuel lines supplies the fuel to the pilot. The two other fuel lines feed the top and bottom fuel circuits for the main mixer. A torch ignitor is located inside the combustor to ignite the fuel–air mixture. All of the air, fuel, and water flows to the test rig are individually metered and controlled. Below is a list of various flows to the test rig:

1. Air flow
    a. Siren air flow into combustor
    b. Siren bypass air flow into combustor
    c. Combustor window purge air
    d. Vessel cooling bypass air

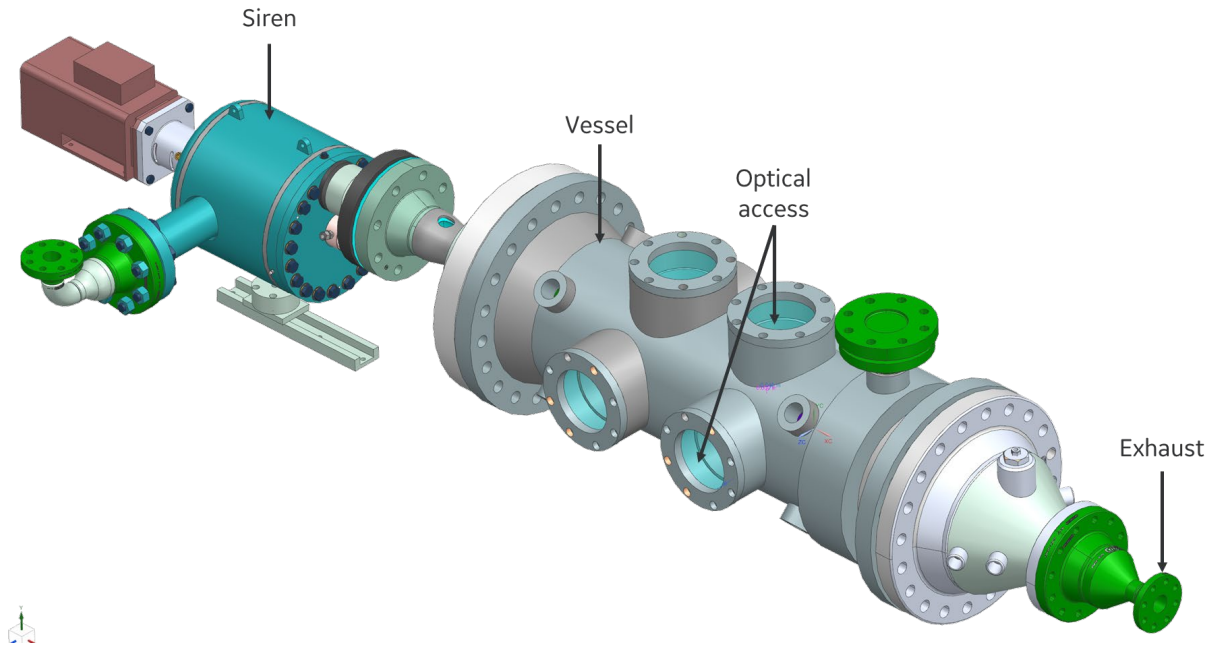

Figure 3. THOR rig siren and pressure vessel assembly employed for the ASCENT Experimental Campaign 2. The vessel features several optical ports suitable for the different diagnostics used in the campaign.

2. Fuel flow
    a. Pilot fuel
    b. Main mixer top fuel
    c. Main mixer bottom fuel
3. Water flow
    a. Siren cooling water
    b. Test article cooling water
    c. Exit orifice cooling water
    d. Pressure vessel reducer cooling water

One can control the static pressure inside the combustor test article by changing the inlet flow pressure (p_3) and the back pressure at the exit. A back pressure valve is employed at the exit of the THOR rig to set both the combustor pressure and the appropriate dome pressure drop ($\mathrm{d}p/p_3$). The THOR rig is instrumented with numerous thermocouples, pressure sensors, and flowmeters to monitor the hardware integrity and operating conditions of interest. The data generated by these sensors are read by a high-speed data acquisition and control system (National Instruments). Dynamic pressure sensors (PCB) were located axially along the mid-plane at specific locations along the test article (see Task 3) for monitoring combustion dynamics and for measuring the acoustic flame transfer function (FTF). A multi-physics model (COMSOL) was employed to fine tune the location of the dynamic sensors to encompass the frequency range of measurements for the multi-microphone method.

A major objective of Experimental Campaign 2 is to characterize the various coupling mechanisms between fluctuations in velocity ($\vec{u}'$), heat release (q'), fuel (or equivalence ratio ϕ'), and pressure (p') for the LPP combustor. Lean pre-mixed pre-vaporized systems are inherently susceptible to combustion-induced oscillations. Practical combustor systems for supersonic flight will need to achieve robust combustor performance over the entire range of supersonic cycle conditions. Understanding component performance and subsequent system interactions is key for early identification of combustion dynamic challenges and solutions.

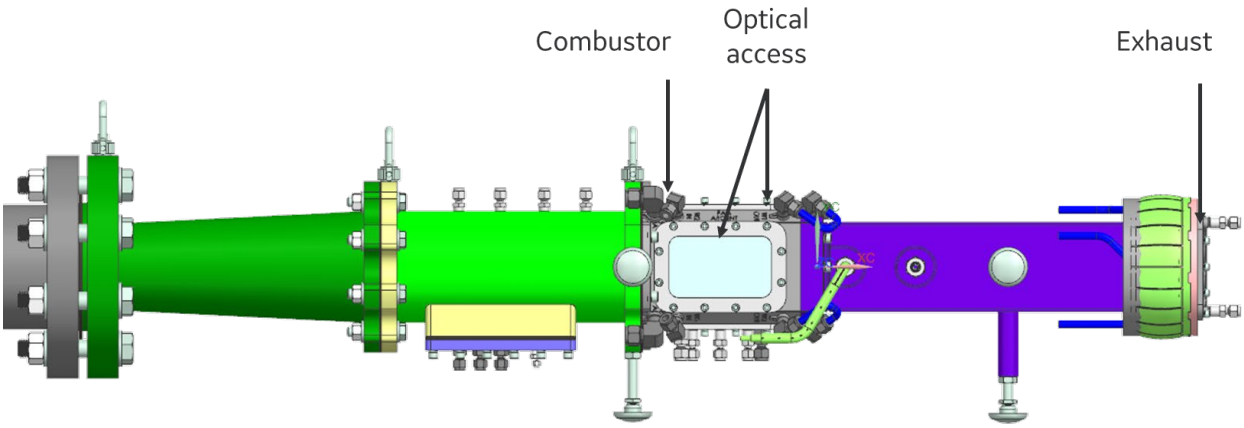

Figure 4. Test article designed for ASCENT 74 Campaign 2.

To this end, the device shown on the left of Figures 2 and 3 is a high-pressure siren that can be used to force oscillations in the air flow with different frequencies and amplitudes. FTF measurements – acquired by measuring the flame response to forcing – enable combustor dynamic performance characterization and provide important insights into the acoustic–heat release coupling. Moreover, the FTF provides key data for validating both analytical and higher-fidelity models for design tools. Hence, FTF measurements were an important focus of Experimental Campaign 2.

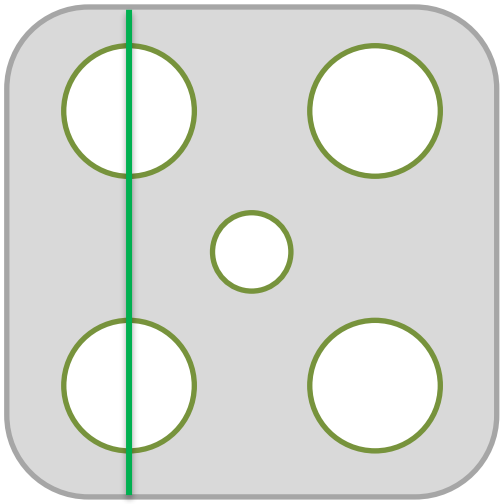

Figure 5. Combustor geometry with the laser sheet position indicated by a green line. The four corners contain the partially pre-mixed bluff-body-stabilized main flames. The bluff-body geometry has been redacted.

The siren device is employed to modulate the frequency of the air sent to the pre-mixer. By varying the rotational speed of the electric motor to the siren device, the modulation frequency can be tuned from 1 to 1050 Hz. The forcing amplitude is controlled through the split between the combustor air that flows through the siren versus through a bypass. In general, a higher mass flow through the siren results in a higher forcing amplitude. One can dynamically change the forcing amplitude by bypassing the flow to the siren and mixing the bypassed (unforced) flow with the forced flow downstream of the siren and upstream of the pre-mixer. The forcing amplitude is monitored and set by dynamic pressure sensors located upstream of the pre-mixers.

Shakedown experiments were undertaken to screen for combustion dynamics behavior, and test conditions were appropriately chosen to coincide with specific operating points of relevance from Experimental Campaign 1 during the previous reporting period. The conditions chosen for this campaign were fixed to the same combustor pressure and equivalence ratios as Campaign 1, but different air preheat temperatures were employed because high-amplitude combustion dynamics behavior was generally observed only at lower air preheat temperatures. Acoustic and optical FTFs and various optical diagnostic measurements were obtained at a fixed air mass flow rate over a range of fuel/air ratios, corresponding to thermal powers of $P_{th} = 0.32 - 0.4$ MW in the pre-mixed main flames. Table 1 provides a summary of the measurements obtained during Campaign 2. Variations in inlet air temperature also helped to ascertain the impact of fuel evaporation on the combustion behavior.

Table 1. Summary of operating conditions. CL: chemiluminescence; FTF: flame transfer function; PLIF: planar laser-induced fluorescence; SPIV: stereoscopic particle image velocimetry.

p_3 (psia)	T_3 (F)	dp/p_3 (%)	P_{th} (MW)	FTF, Acoustic	FTF, Optical	SPIV	OH PLIF	OH* CL	Fuel PLIF
115	670	3.7	0.36–0.40	Yes	No	No	Yes	Yes	Yes
115	550	3.7	0.32–0.44	Yes	Yes	Yes	No	Yes	Yes

Design, Calibration, and Deployment of Diagnostics

Measurements during Experimental Campaign 2 consisted of the following:

1) Dynamic pressure transducer measurements with which to characterize the combustor acoustics and measure FTFs (see Task 3)
2) High-speed stereoscopic particle image velocimetry (SPIV) to measure the velocity field dynamics
3) High-speed OH* chemiluminescence (CL) and OH PLIF to measure the flame dynamics
4) Aromatic PLIF at a repetition rate of 10 Hz to measure the fuel vapor distribution

In addition to these new measurements, work that started in Year 1 was completed to calibrate laser-induced incandescence (LII) measurements of nvPM for the conditions in this combustor. However, LII measurements were de-scoped from Campaign 2 in favor of more detailed flow and flame diagnostics due to the low levels of nvPM measured in Campaign 1. Moreover, based on results from the LES activities (see Task 2), the team decided to add phase Doppler particle analysis and exhaust emissions to Campaign 2, which were not in the original scope. These measurements are ongoing at the time of this report.

Deployment of these diagnostics in the GE test cell required significant optical design efforts due to space and operational constraints. For example, the GE test cell comprised different regions to contain the combustor test article and lasers/control systems. Geometric arrangements around the test article were restricted due to interferences with building infrastructure and the need for routine access to the inside of the pressure vessel. Hence, initial activities were conducted in the Ben T. Zinn Combustion Lab at GT to design the optical path, test the configurations, and de-risk the operations at GE. These efforts included optimal configurations for combining and transmitting laser beams with different wavelengths and spatial characteristics between the laser region and test article, optimal configurations for simultaneously forming multiple laser sheets through a single set of telescope optics, and optimal signal collection configurations. The resultant layouts of the laser and test article spaces are shown in Figure 6.

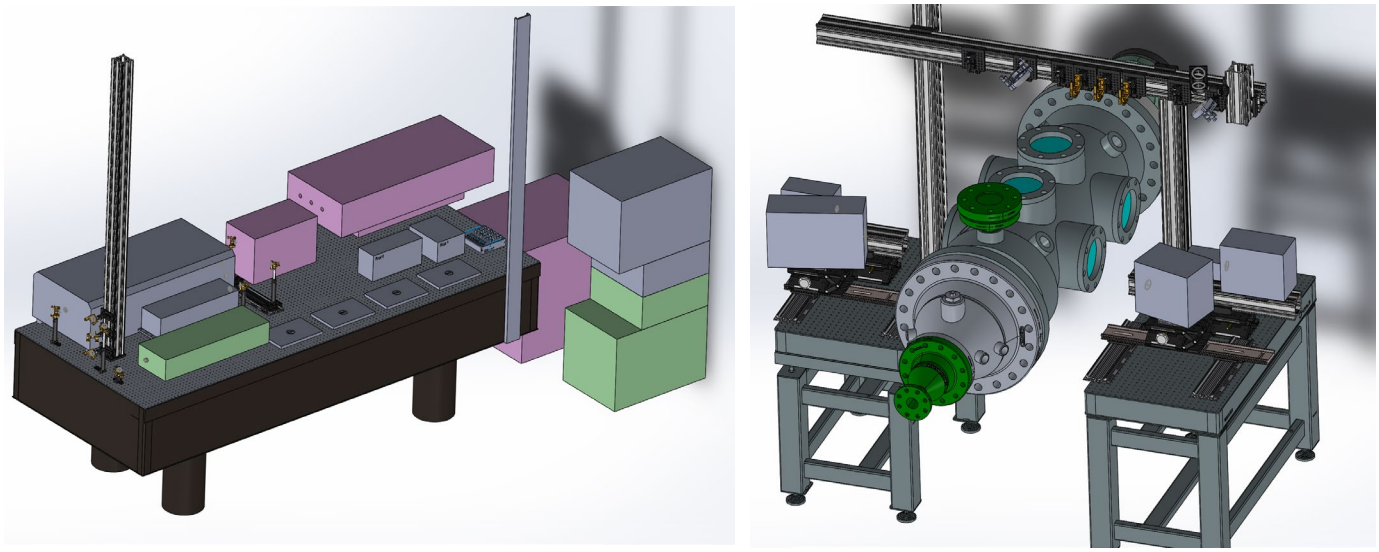

Figure 6. Optical layout in the GE test cell. Left: Laser and control room configuration. Right: Test cell configuration.

CL imaging of OH* at 308 ± 5 nm served as the metric for line-of-sight integrated heat release rate measurements. Previous experiments (Kheirkhah, 2017; Passarelli, 2019) and wide-spectrum measurements from a portable spectrometer (Ocean Optics HR2000) showed that OH* is the most appropriate indicator of heat release rate. A sample spectrum is shown in Figure 7, with the peak corresponding to OH* emissions indicated. The CL images were recorded at a Strouhal number of $St \equiv fD/U = 1.9$ by a high-speed camera (Photron SA-5) coupled to an image intensifier (Invisible Vision, gate time of 50 μs), commercial objective lens (Nikkor 105 mm UV, f/# = 11), and bandpass filter (312 ± 12.5 nm). Here, f is the recording frequency, D is the pre-mixer diameter, a**nd U is the average axial speed of the gas exiting the pre-mixer.**

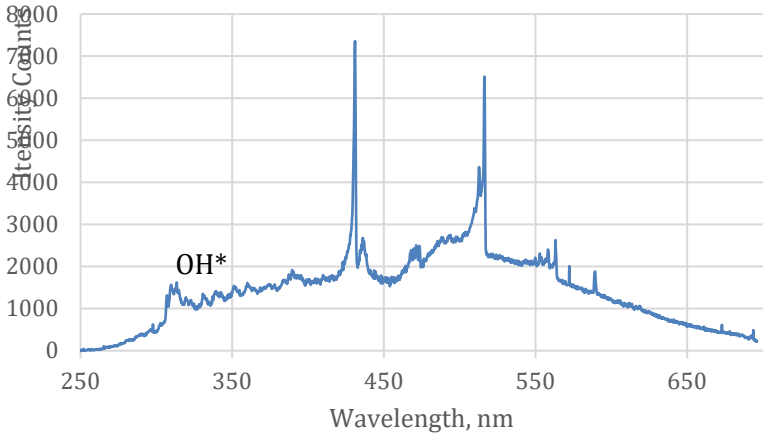

Figure 7. Sample spectrometer readings with the OH* peak indicated.

Qualitative measurements of the fuel mixing behavior were obtained via PLIF of the aromatic species naturally present in the Jet A fuel. The flow was illuminated at a repetition rate of 10 Hz using the fourth harmonic (266 nm) output of an Nd:YAG laser (Spectra Physics Quanta-Ray PRO 350). Laser-induced fluorescence was collected using an intensified camera (Andor, gate time of 100 ns) with an objective lens (Nikkor 105 mm UV, f/# = 4.5) and a two-filter setup consisting of a bandpass (340 ± 40 nm) and a steep-edge long wave pass filter (325 ± 3.5 nm). This filter setup was chosen to align with the center of the fluorescence spectrum of kerosene vapor (Orain, 2014) while simultaneously blocking the signal from OH* CL. Simultaneous shot-to-shot beam profile measurements were obtained by using a phosphorescence plate. The plate was

placed in the path of residual transmission from the 266-nm sheet through the final mirror above the combustor. This low-intensity copy of the sheet induced phosphorescence on the plate, which was then imaged with a separate camera system (FLIR Blackfly USB3). The PLIF images were processed for spatial calibration, background removal, intensifier white-field response, shot-to-shot laser sheet intensity and profile variations, and laser power absorption through the medium.

To characterize the flow field inside the combustor, a double-pulsed, two-camera SPIV setup was used at $St = 0.95$. A high-speed 532-nm Nd:YAG laser (Quantronix) illuminated the flow with pulse separation times varying between 5 and 8 μs and a laser sheet thickness of approximately 2 mm near the beam waist. Mie scattering from nominally 1-μm ZrO_2 tracer particles that were seeded was collected into the two SPIV cameras (Phantom), each equipped with bandpass filters (532 ± 2.5 nm), objective lenses (Tamron 180 mm, f/# = 5.6), and Scheimpflug adapters. While the Stokes number of the tracer particles was too high to track the small-scale features of the flow, the particles were sufficient for measuring the larger-scale, thermoacoustically coupled flow dynamics of interest here. Vector processing was performed using a multi-pass algorithm with an adaptive window shape and size and an iterative vector filter in commercial software (LaVision). Spurious vectors were identified and removed from the vector fields by a median filter outlier detection algorithm. Any remaining gaps in the gas-phase dataset were filled using gappy proper orthogonal decomposition (Saini, 2016).

The OH PLIF excitation system consisted of a frequency-doubled dye laser (Sirah), pumped by an Nd:YAG diode-pumped solid-state laser (EdgeWave). The dye laser system was tuned to excite the $Q_1(7)$ line of the A-X (1,0) transition of OH at 283.2 nm, with a pulse energy of approximately 0.5 mJ/pulse at $St = 0.95$. The OH fluorescence signal was captured by a high-speed CMOS camera (Photron) combined with an image intensifier (UVi). Note that the OH PLIF data are still being analyzed and are not discussed here.

Pressure fluctuations were measured by dynamic pressure transducers (PCB), mounted to the ends of calibrated waveguides in a semi-infinite loop configuration; see Task 3 for details of the pressure measurement locations. A data acquisition system (National Instruments) recorded the pressure and camera timing signals at a sampling rate of 100 kHz.

In addition to the diagnostic setup for Experimental Campaign 2, activities were undertaken during this performance period to analyze the LII data acquired in Campaign 1 (during the previous performance period). This activity will support future experimental campaigns involving LII measurements of nvPM, other projects within ASCENT, and the general scientific community's ability to measure nvPM in high-pressure combustors; the development and validation of methods for measuring soot particle sizes and volume fractions are essential for quantifying the nvPM created during the combustion of Jet A fuels at high pressure. Thus, we validated time-resolved LII (TiRe-LII) measurements using direct soot sampling techniques in order to enable the use of TiRe-LII for direct, non-intrusive nvPM particle sizing.

During this performance period, we focused on the development of a custom soot sampling system that uses transmission electron microscope (TEM) grids to directly sample soot from a small pre-mixed, pre-vaporized calibration burner (Manikandan, 2022). This small burner runs with Jet A fuel, a methane pilot flame, and nitrogen crossflow. The soot sampler operated inside the pressurized burner and was able to rotate TEM grids quickly through the flame to quench and capture soot particles. The grids were then analyzed in a TEM, and soot particle diameters were extracted. In these photos, several features were noted. First, the number of soot particles per agglomerate was higher (>200) than that noted in previous work with ethylene. Second, in some cases, soot restructuring was observed. This restructuring could be due to the exposure of soot particles to water, sulfuric acid, or other combustion products. Third, several mineral-like or fiber-like structures were noted and attributed to S, Fe, or Ca/P, which are commonly found in Jet A fuel (Baldelli, 2020).

While the soot samples were collected, TiRe-LII videos were also captured. For this imaging diagnostic (Chen, 2018; Passarelli, 2022) a 1,064-nm laser was shaped into a 2 x 26 mm sheet with a fluence of 0.08 J/cm^2. This beam was shaped into a top-hat profile and relay-imaged onto the combustor. The resulting incandescence signal was measured by an ultra-high-speed camera (Shimadzu, 10 million frames per second, 55-ns exposure). The decay profiles from each pixel in the image were then extracted and fitted to the LII model developed last fiscal year. This model neglects sublimation due to the low laser fluences used and includes additional terms to capture the shielding effect of large soot agglomerates.

Examples of the data captured by these two techniques are illustrated in Figure 8. For initial validation testing, fuel–air ratios ranging from 0.13 to 0.26 were tested at atmospheric pressure, 1.4 bar, and 2.8 bar. Histograms of these measurements are shown in Figure 9. The results of the two methods agree well, with the average particle size from both measurements on the order of 12–18 nm. This size range matches with prior Jet A soot sampling measurements reported in the literature (Liati, 2019). Using the validated model and TiRe-LII technique, we aim to conduct measurements inside various high-pressure turbine combustors.

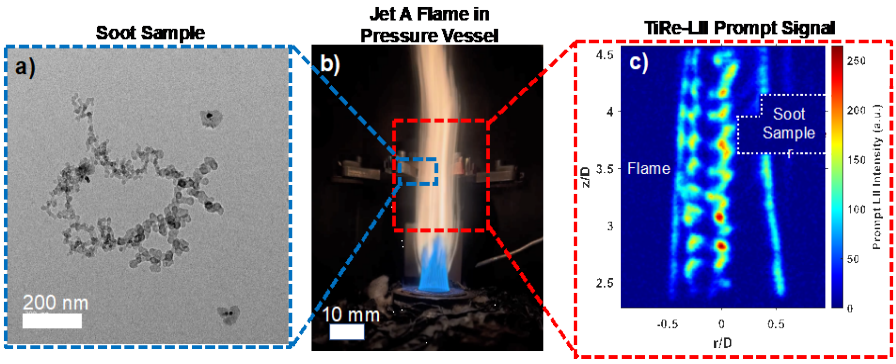

Figure 8. Validation of non-intrusive optical TiRe-LII soot particle sizing with soot sampling measurements in a Jet A flame. The soot sampling mechanism can be seen behind the flame in the center image. TiRe-LII: time-resolved laser-induced incandescence.

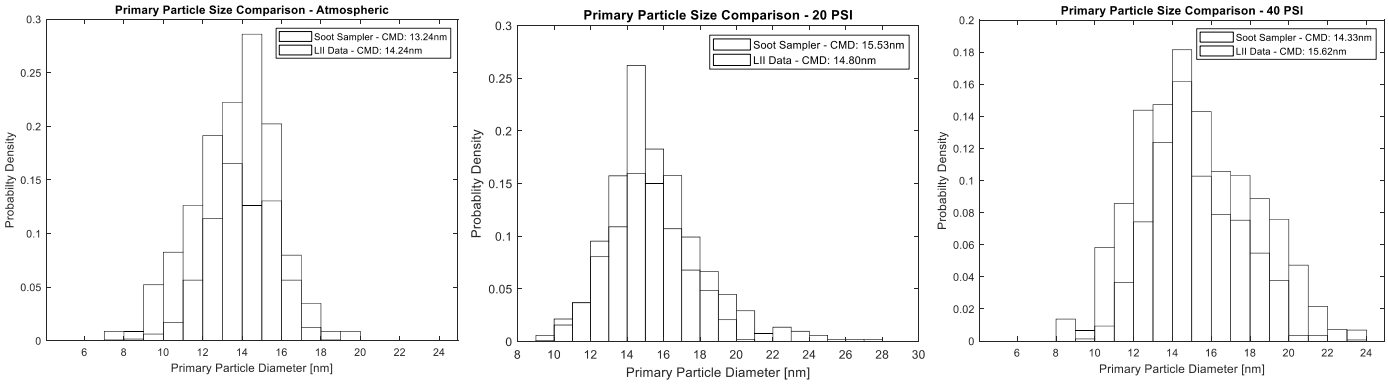

Figure 9. Comparison of soot particle mean diameter (CMD) measured from time-resolved laser-induced incandescence (TiRe-LII) measurements and direct soot sampling show good agreement for atmospheric pressure, 1.4-bar, and 2.8-bar environments.

Experimental Campaign 2

Combustor and Operating Conditions

As described above, Experimental Campaign 2 was performed at GE Research in Niskayuna, NY with the ASCENT 74 test article installed in the THOR rig (Figures 2–5). Each main flame operates under fuel-lean conditions, burning partially pre-vaporized and pre-mixed Jet A fuel. For the laser diagnostics described below, the laser sheet passed through the centers of the main flames on one side of the combustor, as indicated in Figure 5. Prior to data acquisition, the combustor was allowed to settle to steady state, as verified by an examination of static pressure, thermocouple, and mass flow rate measurements.

Data Analysis and Results

Analysis of data from Campaign 2 is ongoing; sample results are presented here. Thus far, the majority of the combustor dynamics analysis has employed spectral proper orthogonal decomposition (SPOD) and phase conditioning. SPOD, which can be applied to any of the high-speed data (OH*, SPIV, etc.), is a modification to classical POD (Sirovich, 1987), wherein a sliding lowpass filter is applied along the diagonals of the correlation matrix before the temporal coefficients are calculated via eigenvalue decomposition (Sieber, 2016). This filtering operation effectively constrains the resulting modes to distinct frequency bands. Unlike traditional filtering operations, such as bandpass filtering the data or phase-averaging the POD modes, the filter in SPOD does not cause any loss of information: the energy outside of the frequency band for a given mode

is redistributed to other modes. SPOD is also more robust to nonstationarity in the data than other spectral decomposition techniques, such as dynamic mode decomposition (DMD (Schmid, 2010; Tu, 2013; Jovanovic, 2014; Roy, 2017), which can experience severe mode splitting. Sieber *et al.* drew a connection between DMD and SPOD, stating that SPOD is similar to a temporally sliding DMD (Sieber, 2016). Figure 10 illustrates the general procedure used to identify and extract the dynamics at the dominant frequencies in the data.

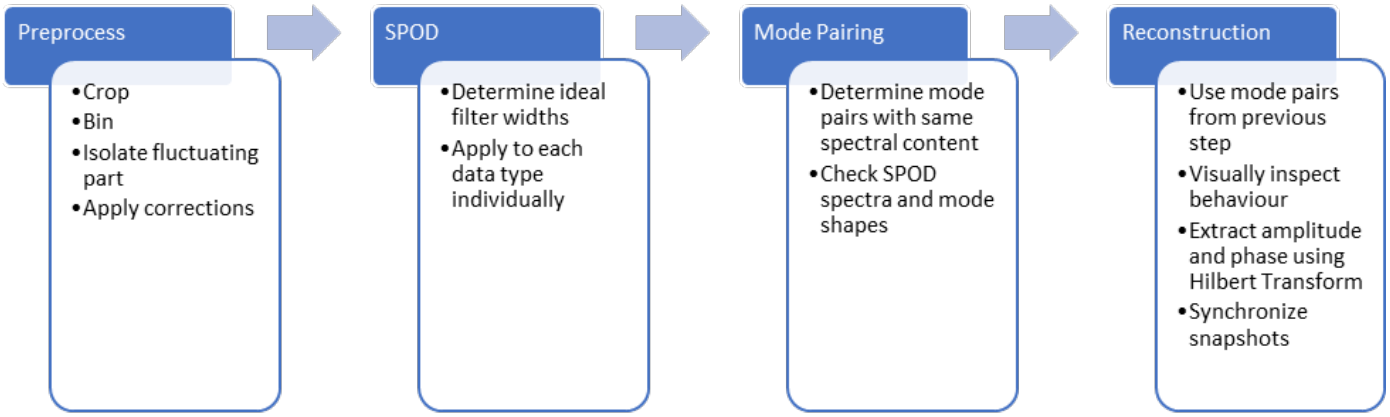

Figure 10. General mode isolation procedure. SPOD: spectral proper orthogonal decomposition.

SPOD is applied following fairly standard data preprocessing. Based on the work by Sieber *et al.* (2017), a Gaussian finite impulse response filter whose standard deviation yields the same cut-off frequency as a box filter with half the length was implemented for SPOD. The third step of this procedure uses the automatic pairing algorithm developed by Sieber *et al.* (2016). This algorithm computes the harmonic correlation or spectral coherence between each mode pair to detect modes with the same spectral signature, but offset by π/2 in phase. As with classical POD, the appearance of modes with similar energy and spectral content but lagging by π/2 radians indicates the presence of coherent oscillatory structures in the data. Thus, the SPOD modes with the strongest harmonic correlation are paired to identify such coherent structures. These mode pairs are then used in the final step to reconstruct the coherent dynamics they represent.

To select the filter widths, the SPOD spectra and spectral content of the modes were examined for filter widths varying from 0 (POD) to the full length of the dataset (effectively a discrete Fourier transform). The ideal filter width is one that yields the fewest modes (or highest energy per mode) with the least amount of mode blending (when one mode contains information at several frequencies).

In addition to SPOD, phase-conditioned mean fields were computed. For this step, the phase "clock" is computed as the complex phase angle of the Hilbert transform of the combustor pressure signal. During data acquisition, a signal from each optical measurement is acquired, indicating the time of each optical frame, which can then be cross-referenced against the phase of the clock. The clock signal and corresponding optical measurements were divided into eight equal phase bins; phase-correlated mean fields for each phase angle were computed from the optical measurements in each bin.

The mean fuel PLIF signal for cases with $P_{th} = 0.40$ MW at different forcing frequencies is shown in Figure 11. Frequencies were normalized to the Strouhal number, $St = fD/U$, as described above. No significant qualitative differences in mean fuel distribution were observed across the different forcing frequencies, indicating no bifurcation in overall flame or flow structure as the system is forced. This observation also held for different thermal powers, corresponding to a leaner FAR.

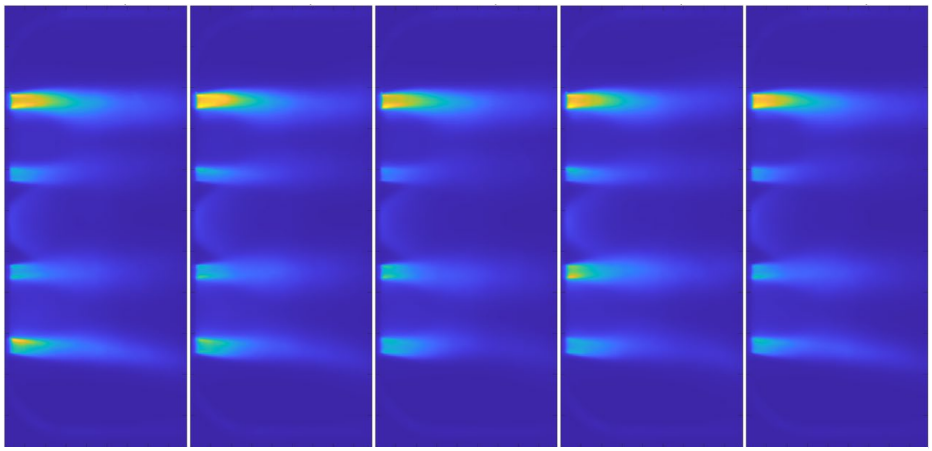

$St = 0.056$ $St = 0.094$ $St = 0.13$ $St = 0.17$ Unforced

Figure 11. Mean fuel planar laser-induced fluorescence fields for $P_{th} = 0.40$ MW at different forcing frequencies.

As will be discussed below, the combustor shows the strongest response to forcing at $St \approx 0.13$. Figure 12 shows mean fuel PLIF fields for $St \approx 0.13$ forcing cases, across different thermal powers. As the FAR decreases, unburnt fuel is measured in the recirculation zones behind the combustor bluff bodies and farther downstream. This observation is indicative of local extinction along the inner shear layer between the reactants and the recirculation zone, allowing mixing of unburnt reactants. This trend is also indicative of a more axially distributed heat release. The phase-conditioned mean fuel PLIF fields at different phases of the pressure cycle (not shown here) did not demonstrate any coherent oscillations in the fuel flow for any combination of thermal power and forcing frequency. Hence, heat release oscillations at the flame do not appear to be due to an oscillating equivalence ratio; rather, heat release oscillations are anticipated to arise from velocity coupling. Thus, a detailed analysis of the velocity dynamics is needed.

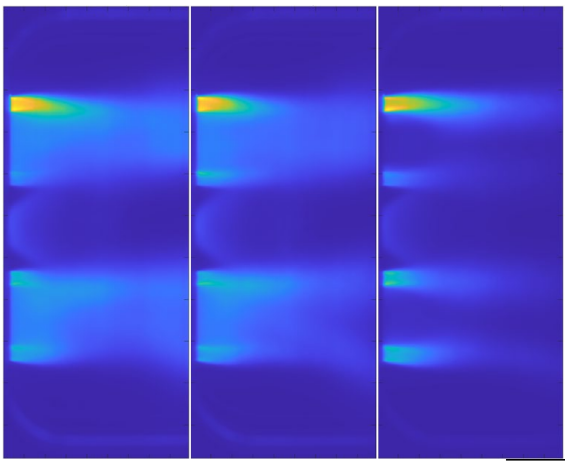

$P_{th} = 0.32$ MW $P_{th} = 0.36$ MW $P_{th} = 0.40$ MW

Figure 12. Mean fuel planar laser-induced fluorescence fields at different FAR values for $St = 0.13$.

Figure 13 shows the mean velocity fields for different forcing frequencies and without forcing at $P_{th} = 0.36$ MW. The vector arrows show in the in-plane velocity, while the background colormap indicates the out-of-plane velocity. All absolute velocity scales have been removed for proprietary reasons. Similar to the fuel PLIF fields, there are no major qualitative changes in the velocity field as the system is forced. The largest difference is that the unforced case has a slightly higher swirl velocity in the downstream region compared with the forced cases. No major changes in mean flow structure have been observed at the different thermal powers in any of the data processed thus far.

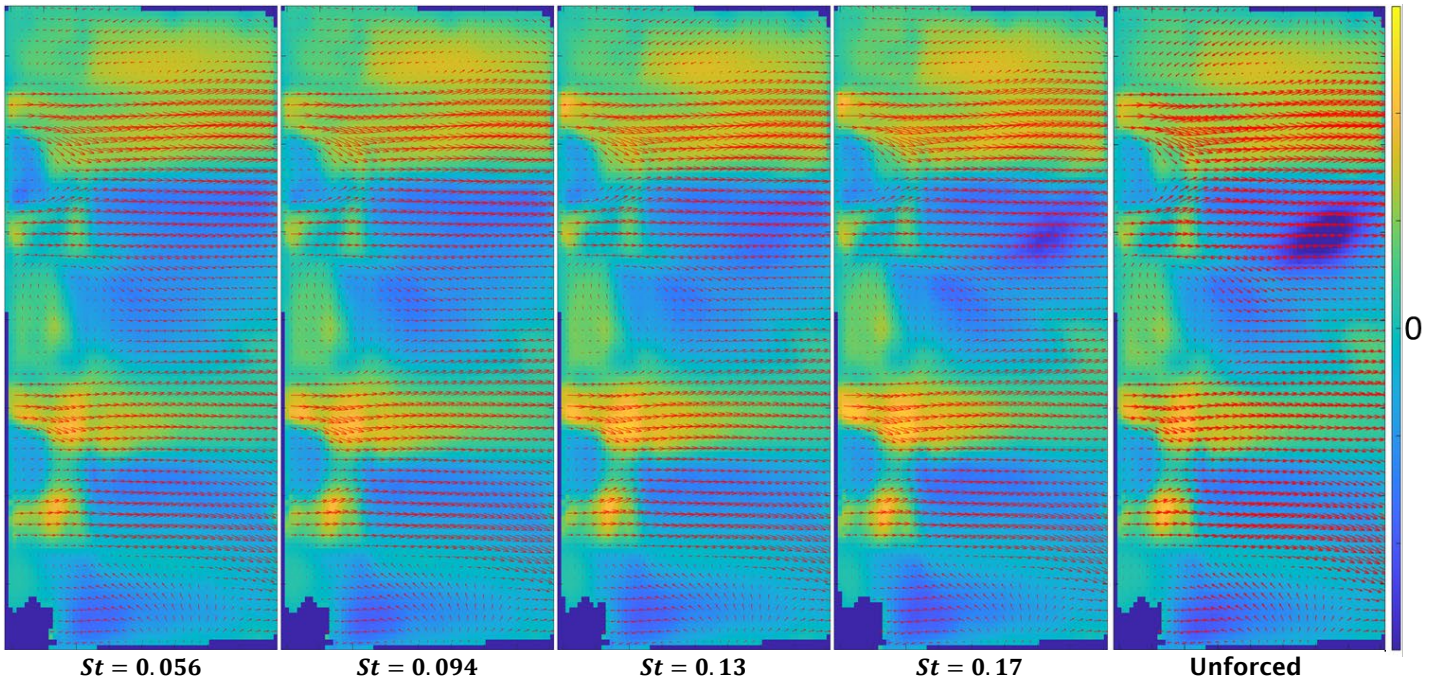

Figure 13. Mean velocity fields for $P_{th} = 0.40$ MW. Vector arrows are the in-plane velocity, and the background is the out-of-plane velocity, with blue and yellow indicating positive and negative velocities, respectively.

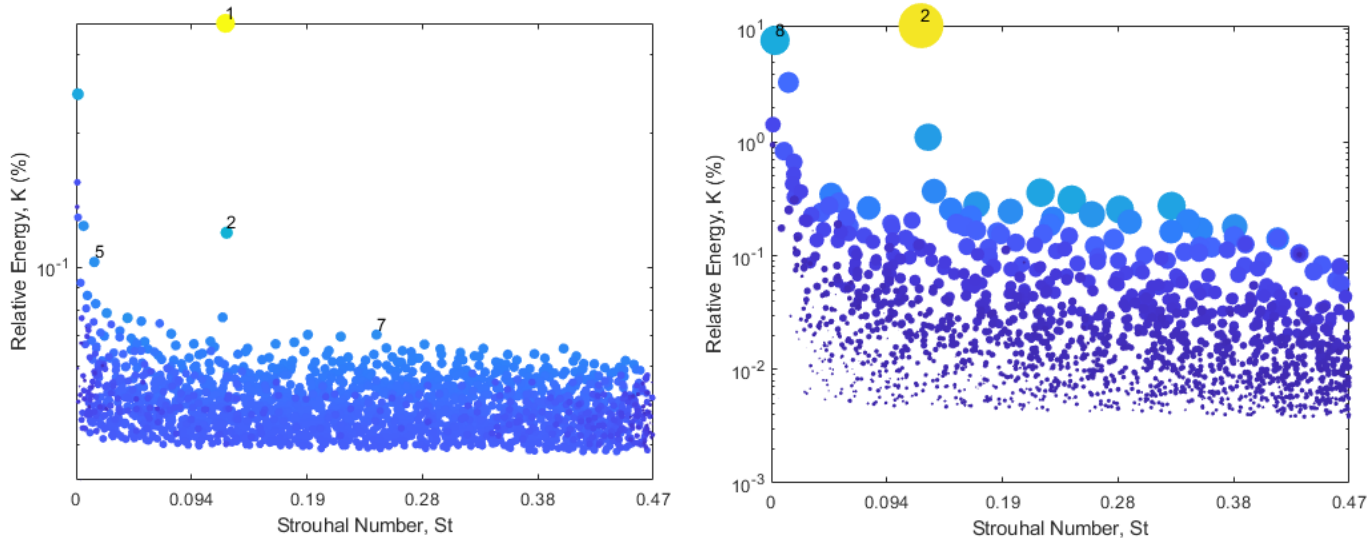

Figure 14. Spectral proper orthogonal decomposition spectrum of stereoscopic particle image velocimetry (left) and OH* chemiluminescence (right) data at $P_{th} = 0.40$ MW without forcing.

To investigate the self-excited and forced velocity field dynamics, SPOD was applied to the SPIV and OH* CL data. The SPOD spectra for the unforced $P_{th} = 0.40$ MW case are shown in Figure 14. Each dot in the SPOD spectrum represents a coherent pair of basis modes. The vertical position of the dot represents its relative contribution to the flow (in the sense of velocity fluctuation magnitudes), and the size/color of the dot represents the relative spectral coherence of the modes making up the pair; high-energy coherent mode pairs are indicated by large dots with a high vertical position.

The dominant feature of the SPOD spectra are the high-energy, coherent velocity oscillations at $St = 0.12$. This frequency corresponds well to the value of $St \approx 0.13$ used in the forced studies and exhibits a strong response to forcing. It is noted that the OH* CL signal also exhibits dynamics at $St \approx 1$, which is not shown on these plots for clarity. These high-frequency dynamics may be the subject of future study.

Figure 15 shows a time sequence of velocity field reconstructions from the dominant $St = 0.12$ SPOD mode pair in the SPIV data over a typical oscillation cycle. The field of view encompasses only the top half of the combustor for clarity, and the shown velocities represent fluctuations at $St = 0.12$ around the mean field. Periodic vortex shedding from the dome face occurs, predominantly in the outer shear layer between the main inflow and the combustor walls. Preliminary observations indicate that this vortex expands and interacts strongly with the more downstream regions of the flame toward the right side of the field of view. Ongoing analysis is coupling the SPOD-reconstructed velocity and heat release dynamics to elucidate their interaction and validate modeling.

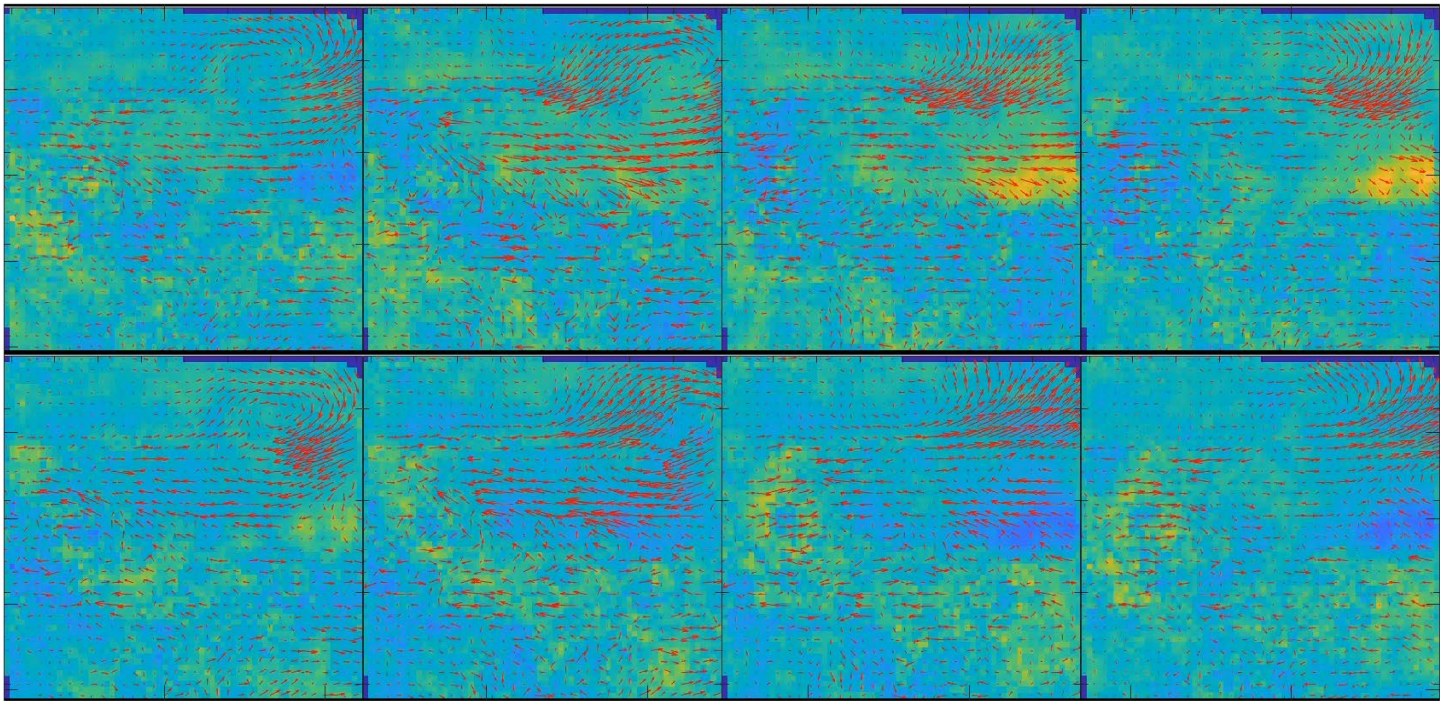

Figure 15. SPOD-reconstructed velocity field dynamics over one oscillation at $\boldsymbol{St = 0.12}$ for an unforced case at $\boldsymbol{P_{th} = 0.40}$ **MW**. The field of view has been cropped to highlight the upper half of the combustor. Vector arrows are the in-plane velocity, and the background is the out-of-plane velocity, with blue and yellow indicating positive and negative velocities, respectively. SPOD: spectral proper orthogonal decomposition.

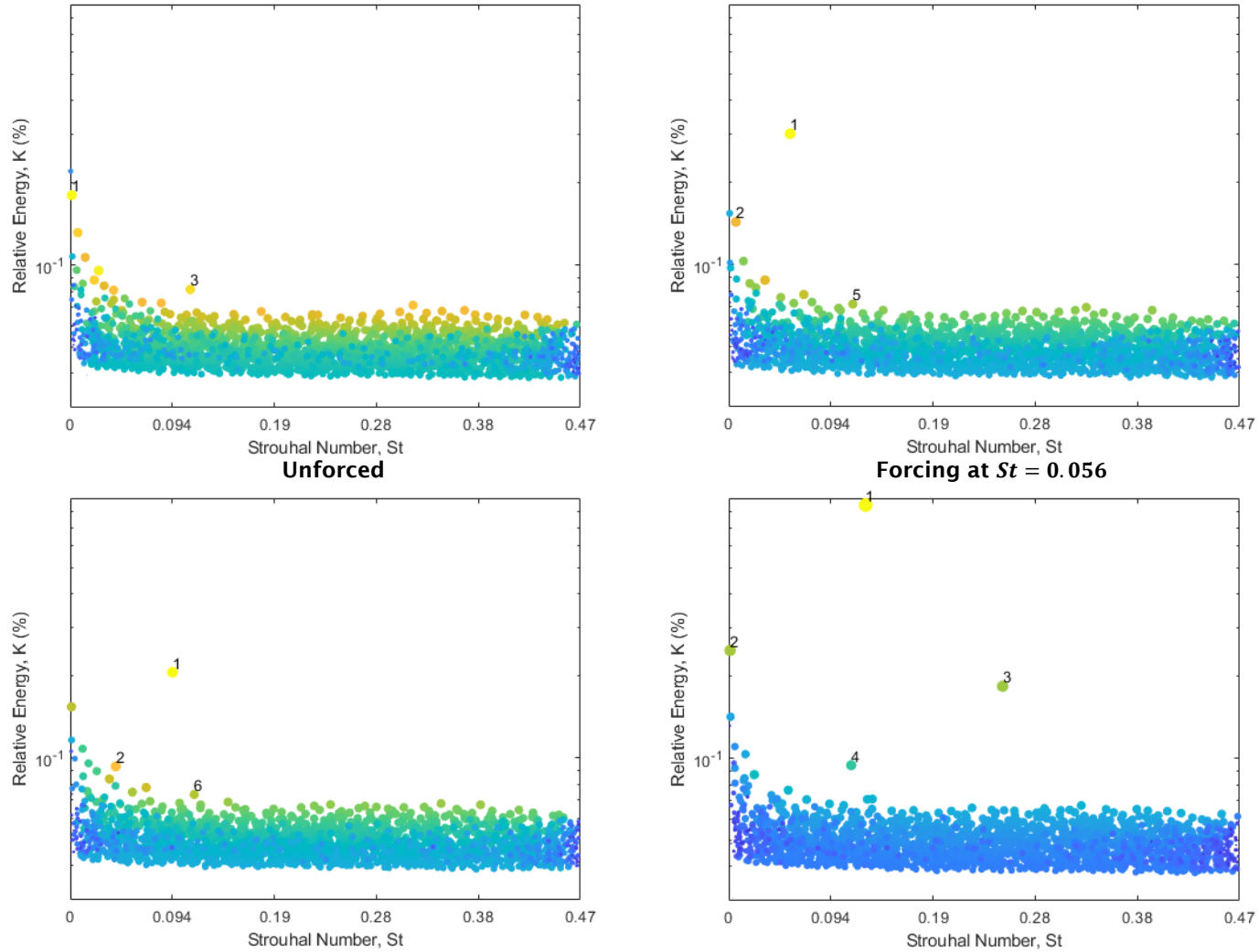

Figure 16. Spectral proper orthogonal decomposition spectra from stereoscopic particle image velocimetry measurements at $P_{th} = 0.36$ MW.

Figure 16 shows SPOD spectra from the SPIV data for the unforced case and with forcing at $St = 0.056, 0.094$, and 0.13 for $P_{th} = 0.36$ MW. The OH* CL spectra are similar and are not included here for brevity. Interestingly, this leaner case does not exhibit the strong self-excited dynamics at $St = 0.12$ observed for the $P_{th} = 0.40$ data. Instead, a signficantly weaker self-excited oscillation occurs at approximately $St = 0.11$. The magnitude of the velocity response to forcing is relatively unchanged between $St = 0.056$ and 0.094, but increases by a factor of approximately five at $St = 0.12$, aligning well with the FTF measurements and analysis in Task 3. Ongoing analysis is investigating the forced velocity dynamics for cases exhibiting stronger self-excited oscillations at $P_{th} = 0.4$ MW.

Milestones

- Campaign 2 test rig design (complete)
- Measurement system design (complete)
- Campaign 2 test rig fabrication (complete)
- Experimental Campaign 2 (complete)

- Data processing from Campaign 1 (complete)
- Data processing from Campaign 2 (on schedule for completion in Q2 2023, 50% complete)

Major Accomplishments

- Design, fabrication, deployment, and operation of a novel LPP combustor
- Advancement of various optical diagnostics for high-pressure gas turbine conditions
- Optical measurements providing insights into combustion dynamics in the LPP combustor

Publications

Published conference proceedings

Passarelli, M. L., Wonfor, S. E., Zheng, A. X., Manikandan, S. R., Mazumdar, Y. C., Seitzman, J. M., Steinberg, A. M., Bower, H., Hong, J., Venkatesan, K., & Benjamin, M. (2022, January 3). Experimental characterization of a lean prevaporized premixed combustor for supersonic transport applications. *AIAA SCITECH 2022 Forum*. AIAA SCITECH 2022 Forum, San Diego, CA & Virtual. https://doi.org/10.2514/6.2022-2347

Passarelli, M. L., Wonfor, S. E., Zheng, A. X., Mazumdar, Y. C., Seitzman, J. M., Steinberg, A. M., Salazar, V., Venkatesan, K., & Benjamin, M. (2023, January 23). Forced and unforced dynamics of a lean premixed prevaporized combustor for civil supersonic transport. *AIAA SCITECH 2023 Forum*. AIAA SCITECH 2023 Forum, National Harbor, MD & Online. https://doi.org/10.2514/6.2023-0920

Zheng, A. X., Manikandan, S., Wonfor, S. E., Steinberg, A. M., & Mazumdar, Y. C. (2023, January 23). Planar time-resolved laser-induced incandescence for particulate emissions in premixed flames at elevated pressures. *AIAA SCITECH 2023 Forum*. AIAA SCITECH 2023 Forum, National Harbor, MD & Online. https://doi.org/10.2514/6.2023-2435

Outreach Efforts

Eight semesters of undergraduate research-for-credit have been associated with this project.

Awards

None.

Student Involvement

- Mitchell Passarelli (PhD Candidate), GT: Mie scattering and OH* CL measurements
- Samuel Wonfor (PhD Candidate), GT: fuel PLIF measurements
- Andrew Zheng (PhD Candidate), GT: TiRe-LII processing of OH PLIF measurements
- Sundar Ram Manikandan (MS Candidate), GT: thermophoretic nvPM sampling system
- Coleman Pethel, Mihir Rao, Andrew Semelka (BS Students), GT: assistance in data processing, calibration burner, diagnostics design, etc.

Plans for Next Period

- Complete processing of data from Campaign 2 (Q2 2023)
- Complete Campaign 3 test rig design, fabrication, and assembly (Q2 2023)
- Perform Experimental Campaign 3 (Q2–3 2023)
- Analyze data from Campaign 3 (Q3–4 2023)

References

Berton, J. J., Huff, D. L., Geiselhart, K., & Seidel, J. (2020, January 6). Supersonic technology concept aeroplanes for environmental studies. *AIAA Scitech 2020 Forum*. AIAA Scitech 2020 Forum, Orlando, FL. https://doi.org/10.2514/6.2020-0263

Speth, R. L., Eastham, S. D., Fritz, T. M., Sanz-Morere, I., Agarwal, A., Prashanth, P., Allroggen, F., & Barrett, S. R. H. (2021). *Global environmental impact of supersonic cruise aircraft in the stratosphere.* https://ntrs.nasa.gov/citations/20205009400

Hassan, M., Pfaender, H., & Mavris, D. (2020, June 15). Design tools for conceptual analysis of future commercial supersonic aircraft. *AIAA AVIATION 2020 FORUM*. AIAA AVIATION 2020 FORUM, VIRTUAL EVENT. https://doi.org/10.2514/6.2020-2620

Kharina, A., MacDonald, T., Rutherford, D. Environmental performance of emergic supersonic transport aircraft. (2018). *International Council on Clean Transportation.*

Niedzwiecki, R. W. (1992). Low emissions combustor technology for high-speed civil transport engines. *NASA. Langley*

Research Center, First Annual High-Speed Research Workshop, Part 2. https://ntrs.nasa.gov/citations/19940028975

Kheirkhah, S., Cirtwill, J. D. M., Saini, P., Venkatesan, K., & Steinberg, A. M. (2017). Dynamics and mechanisms of pressure, heat release rate, and fuel spray coupling during intermittent thermoacoustic oscillations in a model aeronautical combustor at elevated pressure. *Combustion and Flame*, *185*, 319–334. https://doi.org/10.1016/j.combustflame.2017.07.017

Passarelli, M. L., Wabel, T. M., Venkatesan, K., Cross, A., & Steinberg, A. M. (2019, August 19). Experimental analysis of thermoacoustic oscillations in a model aeronautical gas turbine combustor at realistic conditions. *AIAA Propulsion and Energy 2019 Forum*. AIAA Propulsion and Energy 2019 Forum, Indianapolis, IN. https://doi.org/10.2514/6.2019-3949

Orain, M., Baranger, P., Ledier, C., Apeloig, J., & Grisch, F. (2014). Fluorescence spectroscopy of kerosene vapour at high temperatures and pressures: Potential for gas turbines measurements. *Applied Physics B*, *116*(3), 729–745. https://doi.org/10.1007/s00340-013-5756-z

Saini, P., Arndt, C. M., & Steinberg, A. M. (2016). Development and evaluation of gappy-POD as a data reconstruction technique for noisy PIV measurements in gas turbine combustors. *Experiments in Fluids*, *57*(7), 122. https://doi.org/10.1007/s00348-016-2208-7

Manikandan, S.R. (2022). *Experimental characterization of NVPM in a laminar premixed jet flame at elevated pressure using thermophoretic sampling and transmission electron microscopy* [Master's thesis, Georgia Institute of Technology].

Baldelli, A., Trivanovic, U., Corbin, J. C., Lobo, P., Gagné, S., Miller, J. W., Kirchen, P., & Rogak, S. (2020). Typical and atypical morphology of non-volatile particles from a diesel and natural gas marine engine. *Aerosol and Air Quality Research*, *20*(4), 730–740. https://doi.org/10.4209/aaqr.2020.01.0006

Chen, Y., Cenker, E., Richardson, D. R., Kearney, S. P., Halls, B. R., Skeen, S. A., Shaddix, C. R., & Guildenbecher, D. R. (2018). Single-camera, single-shot, time-resolved laser-induced incandescence decay imaging. *Optics Letters*, *43*(21), 5363. https://doi.org/10.1364/OL.43.005363

Passarelli, M. L., Wonfor, S. E., Zheng, A. X., Manikandan, S. R., Mazumdar, Y. C., Seitzman, J. M., Steinberg, A. M., Bower, H., Hong, J., Venkatesan, K., & Benjamin, M. (2022, January 3). Experimental characterization of a lean prevaporized premixed combustor for supersonic transport applications. *AIAA SCITECH 2022 Forum*. AIAA SCITECH 2022 Forum, San Diego, CA & Virtual. https://doi.org/10.2514/6.2022-2347

Passarelli, M. L., Wonfor, S. E., Zheng, A. X., Manikandan, S. R., Mazumdar, Y. C., Seitzman, J. M., Steinberg, A. M., Bower, H., Hong, J., Venkatesan, K., & Benjamin, M. (2022, January 3). Experimental characterization of a lean prevaporized premixed combustor for supersonic transport applications. *AIAA SCITECH 2022 Forum*. AIAA SCITECH 2022 Forum, San Diego, CA & Virtual. https://doi.org/10.2514/6.2022-2347

Sirovich, L. (1987). Turbulence and the Dynamics of Coherent Structures Part I: Coherent Structures. *Quarterly of Applied Mathematics, 45*(3), 561-571.

Sieber, M., Paschereit, C. O., & Oberleithner, K. (2016). Spectral proper orthogonal decomposition. *Journal of Fluid Mechanics*, *792*, 798–828. https://doi.org/10.1017/jfm.2016.103

Schmid, P.J. (2010). Dynamic mode decomposition of numerical and experimental data. *Journal of Fluid Mechanics, 656*, 5-28. doi:10.1017/S0022112010001217

Tu, J.H. (2013). *Dynamic Mode Decomposition: Theory and Applications* [Doctor of Philosophy thesis, Princeton University]. https://cwrowley.princeton.edu/theses/tu.pdf

Jovanović, M. R., Schmid, P. J., & Nichols, J. W. (2014). Sparsity-promoting dynamic mode decomposition. *Physics of Fluids*, *26*(2), 024103. https://doi.org/10.1063/1.4863670

Roy, S., Yi, T., Jiang, N., Gunaratne, G. H., Chterev, I., Emerson, B., Lieuwen, T., Caswell, A. W., & Gord, J. R. (2017). Dynamics of robust structures in turbulent swirling reacting flows. *Journal of Fluid Mechanics*, *816*, 554–585. https://doi.org/10.1017/jfm.2017.71

Sieber, M., Oliver Paschereit, C., & Oberleithner, K. (2017). Advanced identification of coherent structures in swirl-stabilized combustors. *Journal of Engineering for Gas Turbines and Power*, *139*(2), 021503. https://doi.org/10.1115/1.4034261

Task 2 - Large Eddy Simulations of Combustor Operation and Emissions

Georgia Institute of Technology

Objectives

Simulations of advanced propulsion and power systems require a multiscale physics treatment, in turn requiring trade-offs between cost and accuracy. Achieving the optimal balance is complicated due to the nonlinear nature of turbulent reacting flows, which involve multiphase mixtures, highly nonlinear chemical kinetics, multiscale velocity and mixing processes, turbulence–chemistry interactions, compressibility effects (density changes induced by changes in pressure), and variable inertia effects (density changes induced by changes in composition or heat addition). Coupling between processes occurs over a wide range of time and length scales, many being smaller than can be resolved in a numerically feasible manner. Further complications arise when liquid or solid phases are present due to the introduction of dynamically evolving interface boundaries and the resultant complex exchange processes.

The overarching objective of this task is to provide quantitative insights into the accuracy of select calculations and to assess critical trade-offs between cost and accuracy. One set of calculations is performed using preferred engineering LES solvers, with the goal of minimizing cost for a targeted accuracy, as required by industry. A companion set of high-resolution LES calculations are performed using a research solver, the RAPTOR code at GT (Oefelein, 2006; Oefelein, 2018), to provide detailed information beyond that available from the experiments alone. Complementary information from the first-principles LESs and experimentally measured data provides a unique opportunity for elucidating the central physics of turbulent combustion processes in realistic parameter spaces and for making clear assessments of how a given combination of affordable engineering-based models perform. After achieving an adequate level of validation, results from the high-resolution LES calculations will provide fundamental information that cannot be measured directly and that is relevant to the development of lower-order engineering models. Thus, a strong link between theory, experiments, and relevant applications is established. The ultimate objectives of this task are to (a) assess the model fidelity/attributes required to accurately simulate the operability and emissions and (b) assess the trade-offs between accuracy and cost.

Research Approach

The GE combustor operates with liquid Jet A (CAT-A2) fuel delivered through upstream atomizers into bluff-body-stabilized pre-mixers, as well as through a central swirling pilot. Over the initial stages of the project, the GE and GT simulation teams worked toward the development of a common computational domain that enabled detailed treatment and analysis of the rig boundary conditions and operating conditions while also working around proprietary aspects of the GE hardware. A set of calculations in Fluent were performed by GE via standard practice in a computational domain that included the upstream plenum, upstream proprietary liquid-fuel/air injection system, combustion chamber, and exhaust, as shown in Figure 17.

In contrast, due to the proprietary nature of the injection system, the GT LES computational domain begins at the burner inlet planes beginning upstream of the dome that houses the bluff-body-stabilized pre-mixers, as shown in Figure 18. The domain includes all flow features of the pilot and pre-mixers as well as fine features such as wall and dome cooling holes. The major goals of this effort are to (a) establish good correspondence between the GE and GT simulation efforts, (b) establish

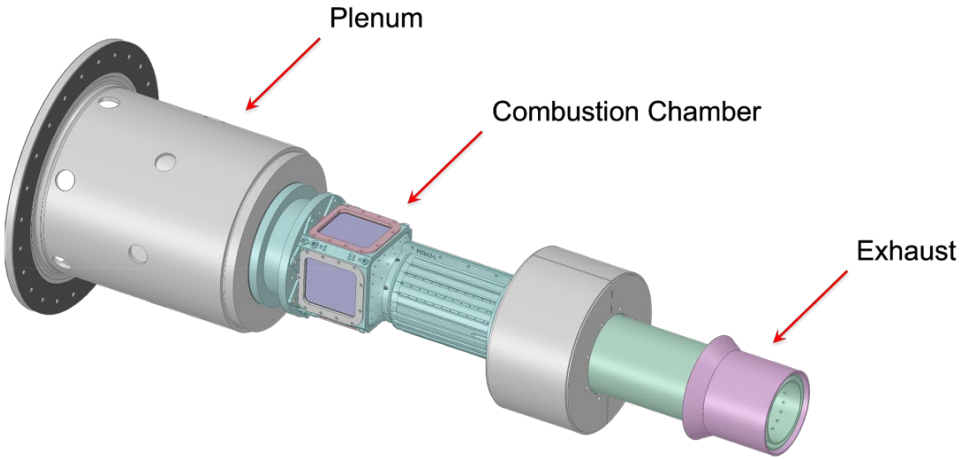

Figure 17. Extended computational domain used for the GE Fluent calculations.

advanced methodologies for the treatment of boundary conditions in “industrial-grade” rigs such as this, and (c) quantify and enable detailed analyses of the impact of both the inner combustion characteristics and the actual physical boundary conditions on the overall operating characteristics of the combustor.

Simulations performed by GT and GE are specifically designed to be complementary, not redundant. GT is performing high-resolution first-principles LESs designed to provide additional levels of information that are directly relevant to assessing, understanding, and improving the current state-of-the-art models being used, with an emphasis on accuracy over cost. The GE Fluent calculations are designed to apply “best-practices” engineering CFD to first establish the benchmark accuracy of the current models used for the conditions of interest here and then systematically assess where improvements can be made. Collectively, the combination of GT and GE calculations enables an advanced engineering workflow to systematically improve the accuracy and confidence of CFD design methodology while minimizing cost.

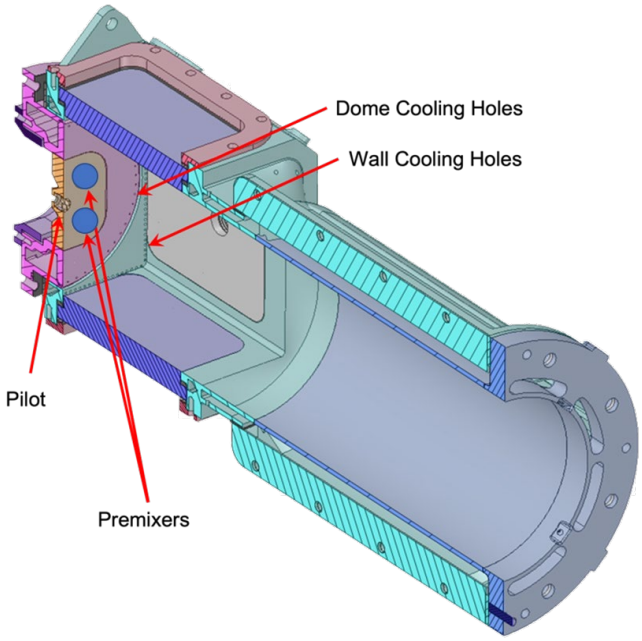

Figure 18. Computational domain used for the large eddy simulation calculations by GT.

Four high-quality production-level grids were designed for the high-resolution LESs performed at GT. The basic topology, which is shown in Figure 19, is identical to the geometry shown in Figure 18. A series of simulations using RAPTOR LES were performed to establish a foundation for comparisons between the codes. Grids composed of 30, 60, 120, and 240 million cells corresponding to the topology shown in Figure 19, were used to obtain detailed solutions at these different resolutions.

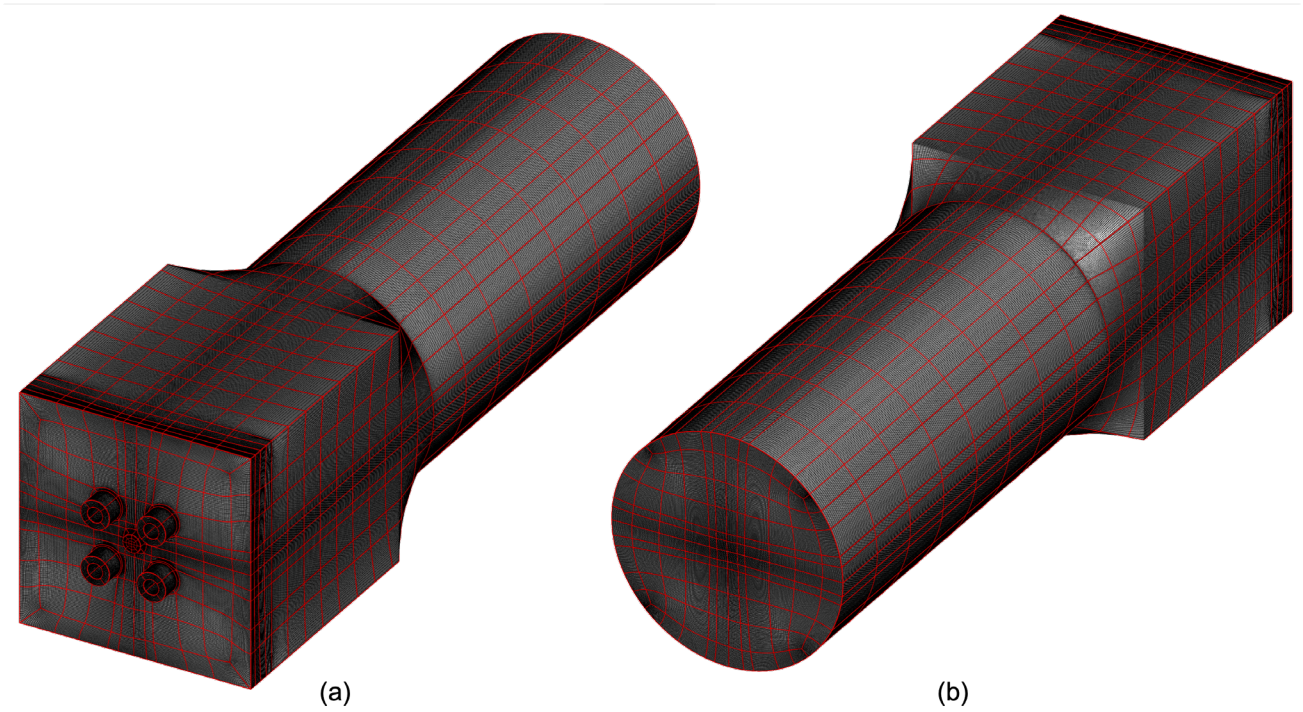

Figure 19. Grid topology used for the RAPTOR large eddy simulation calculations. Grids composed of 30, 60, 120, and 240 million cells were used to assess model performance as a function of resolution.

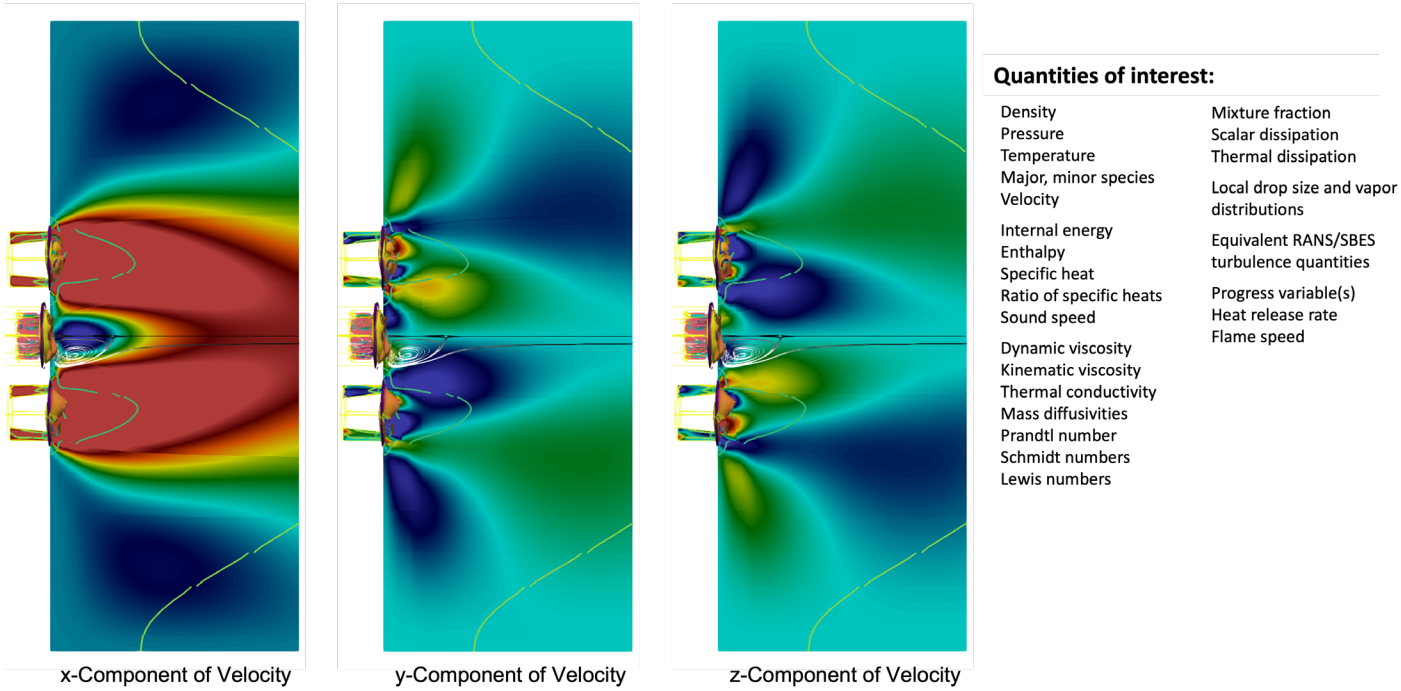

Figure 20. Representative time-averaged velocity from the RAPTOR large eddy simulation code. Quantities of interest being extracted from the simulation include those listed on the right.

Figures 20 and 21 show representative time averages and instantaneous results from the RAPTOR LES code. These results

were obtained by using the detailed treatment of boundary conditions established in Year 1. Time-dependent turbulent inflow profiles are constructed using the synthetic eddy method (Jarrin, 2009). A modified compressible formulation of the synthetic eddy method is employed to provide time-evolving turbulent inflow conditions to capture the physical nonuniformities that are present across the pre-mixer inlet planes. The inputs used to construct the signals are the nonuniform mean velocity profiles, Reynolds stress tensor, and integral scale distributions extracted directly from the GE Fluent calculations, which effectively establish a one-to-one correspondence between the codes and thus minimize uncertainties in the results due to differences in boundary conditions when comparing the interior field quantities of interest. Specific quantities of interest are also listed in Figure 21.

Having established baseline datasets from each of the codes, attention has now focused on joint comparisons between the quantities of interest listed in Figure 21. These data are being extracted from key cross-sectional planes such as those shown in Figure 22. Flow entering the combustion chamber involves a complex combination of turbulent gas-phase fluid dynamics and liquid-fuel spray dynamics. The pre-mixers inject partially pre-mixed gas laden with liquid-fuel drops. The pilot radially injects swirling air flow onto the liquid-fuel jet. The gas-phase flow velocity and liquid-fuel drop size and velocity distributions are found to be nonuniform both within and between the pre-mixers. In addition, the mass flow of air through the dome and wall cooling holes accounts for 40% of the total mass flow, and flow across the wall cooling holes is also nonuniform. Thus, there are many challenges in isolating the effectiveness of the different sub-models used in the simulations.

To isolate different effects, the GT LES is performed over a range of resolutions to quantify the fidelity with which different processes can be represented, either instantaneously or statistically. Figure 23 shows an example in a canonical non-pre-mixed flame that demonstrates this progression. At the finest level of resolution, the simulations emulate structures that are comparable to corresponding Raman–Rayleigh imaging using the exact same color scales and contour thresholds (i.e., the data are processed identically in the same manner). As the local spatial and corresponding temporal resolutions are reduced (which significantly decreases the calculation cost), the simulation can no longer emulate the actual turbulent flame structure. Instead, the simulation can only represent these dynamics from a statistical perspective. The major question then becomes to what degree are the sub-models (either LES or RANS) able to correctly represent the bulk effect of the unresolved processes as a function of these statistical quantities of interest. The progression of GT LES cases is designed to provide the quantitative data required to answer this question by reconstructing modeled terms in the engineering-based GE calculations and comparing them with corresponding reconstructions from the first-principles GT LES. These comparisons will be conducted as part of the tasks performed in Year 3.

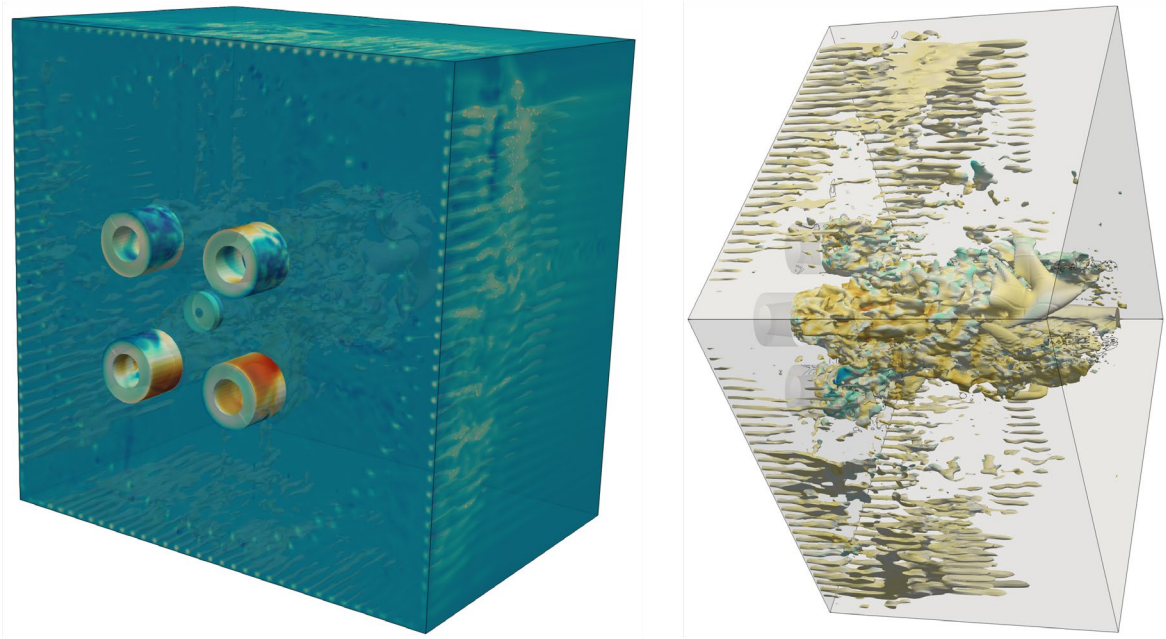

Figure 21. Representative instantaneous fields of temperature and velocity from the RAPTOR large eddy simulation code.

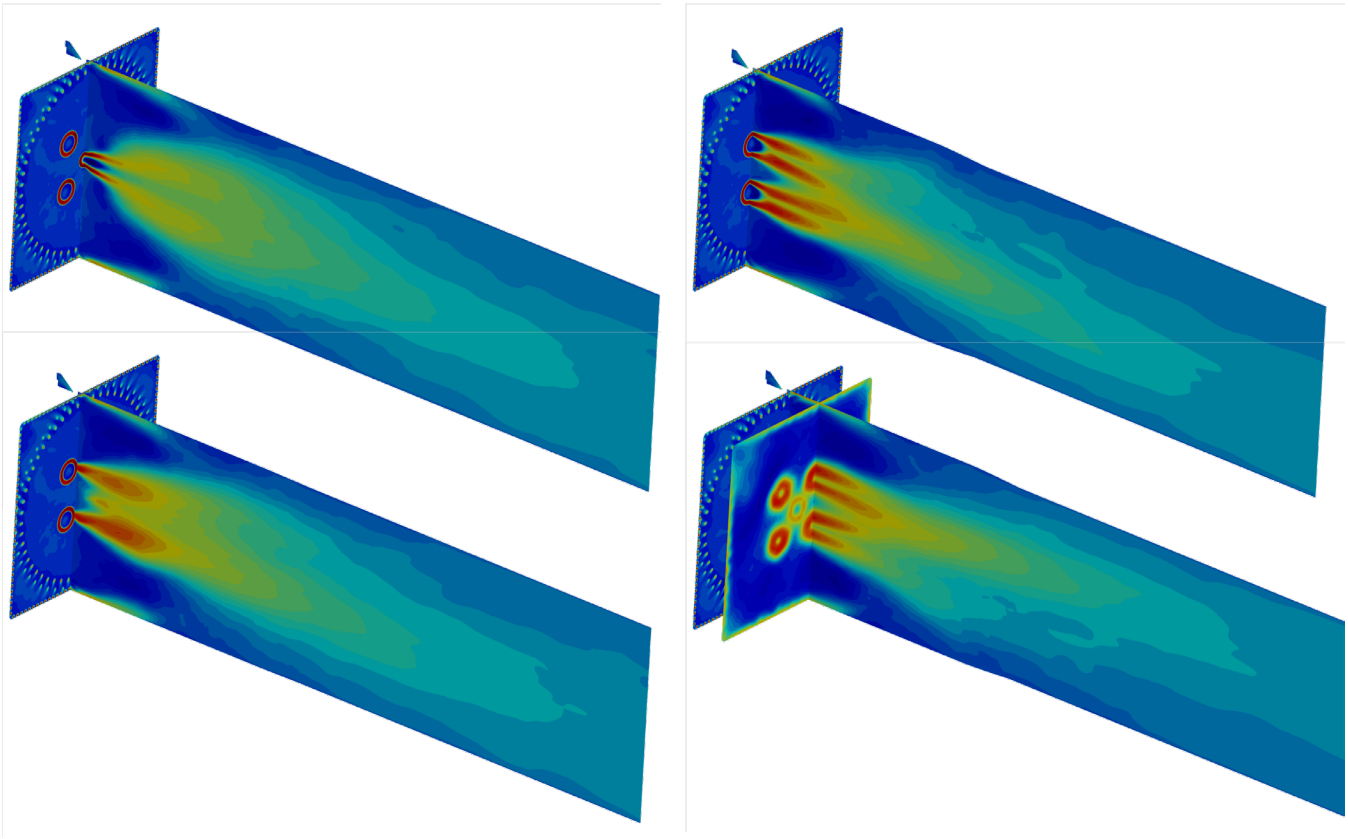

Figure 22. Representative cross-sectional planes of interest for detailed comparisons between GT large eddy simulations, GE Fluent calculations, and measured data. Corresponding line plots within each of these planes will also be extracted to further illuminate key quantitative details.

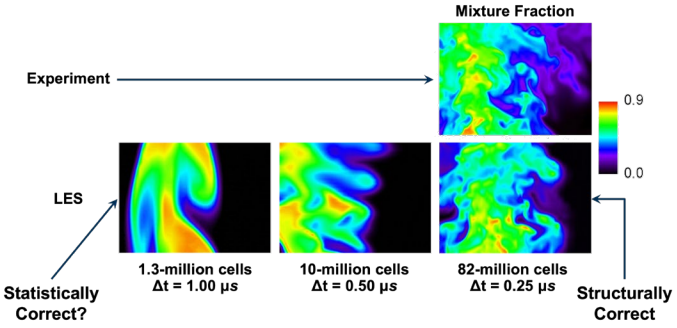

Figure 23. Analysis of a canonical non-pre-mixed flame that demonstrates how simulations at different levels of fidelity represent turbulent structures. At the finest level of resolution, the simulations emulate actual physical structures that are comparable to corresponding Raman–Rayleigh imaging (top right) using the exact same color scales and contour thresholds. LES: large eddy simulation.

In addition to the analysis of gas-phase quantities, recent observations between the experimental results and GE CFD calculations have suggested a discrepancy in the amount of liquid-fuel drops entering the chamber. Imaging within the test article suggests that most of the fuel is fully vaporized as it enters the chamber from the exit planes of the four pre-mixers. Conversely, the CFD predictions indicate a much higher level of liquid-fuel drops entering the chamber. This discrepancy

suggests that inaccuracies may be present in the spray injection models used. Specifically, a typical approximation employed to make the engineering CFD calculations affordable for design is the so-called "parcel method," where groups of drops are represented by a single "parcel" that is injected and tracked. This approach eliminates the need to track millions of physical drops in a simulation at the expense of fidelity in the time-dependent dispersion, mass exchange, and energy exchange characteristics of the spray. To assess the accuracy of the parcel method, a set of simulations are being performed with RAPTOR LES that eliminate the use of parcels and track physical drops using the same injection conditions. This effort will provide detailed quantitative guidelines regarding the maximum number of drops a given parcel can represent in these types of flow configurations. Figure 24 shows representative spray distributions produced using RAPTOR LES. The results are then processed to determine the degree to which GE simulations using parcels with different number densities reproduce the same local distributions in drop size, mass, and temperature.

Tasks performed to date have provided the foundational workflow and data required to enable one-to-one comparisons between the GE CFD and GT LES results, with an emphasis on understanding the accuracy of the engineering models being used in the GE calculations. In addition, this effort has enabled comparisons between the measured and modeled results. Studies planned as part of Year 3 tasks include analyses of (a) sub-model accuracy and performance in a complex geometric environment, (b) turbulent velocity and scalar mixing, (c) turbulent mixed-mode combustion, (d) finite-rate chemical kinetics and combustion dynamics, and (e) engineering model performance and best practices for model implementation.

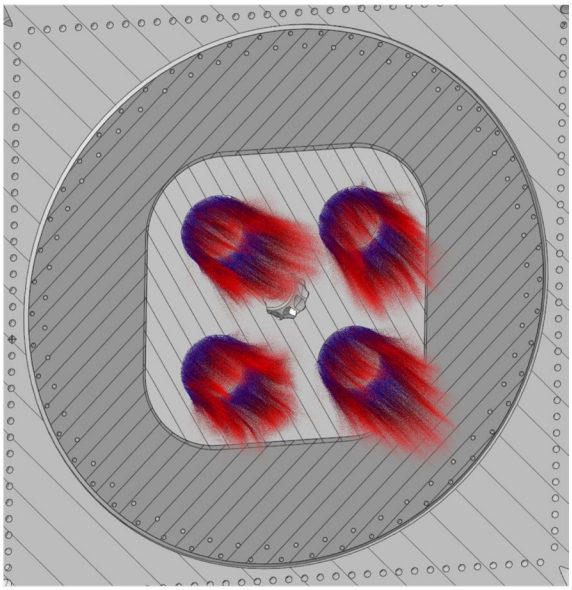

Figure 24. Representative spray distributions produced using RAPTOR large eddy simulations.

Milestones

- Detailed flow field characterization of test article 1 using RAPTOR LES (complete)
- Baseline comparisons of RAPTOR LES with engineering LES of test article 1 (complete)
- Parametric analysis of boundary condition sensitivity (complete)
- Code-to-code comparisons and analysis (test article 1 in progress, 80% complete)

Major Accomplishments

- Fluent LES simulations of the LPP combustor
- Established workflow to align space- and time-dependent boundary conditions between GE Fluent and GT RAPTOR

Publications

None.

Outreach Efforts

Four semesters of undergraduate research-for-credit have been associated with this project.

Awards
None.

Student Involvement
- Sriram Kalathoor (Graduate Research Assistant, PhD Candidate), GT: baseline calculations with RAPTOR code.
- Neilay Amin, Preethi Mysore, Katrina Potak, and Rachel Wilder (BS Students), GT: assistance in setting up grids, boundary conditions, and computational runs

Plans for Next Period
- Apply workflow and data analysis techniques developed to test article 2 (Q3 2023)
- Perform a detailed comparison of RAPTOR LES, Fluent LES, and experimental measurements of test article 2 (Q3–4 2023)

References
Oefelein, J. C. (2006). Large eddy simulation of turbulent combustion processes in propulsion and power systems. *Progress in Aerospace Sciences*, *42*(1), 2–37. https://doi.org/10.1016/j.paerosci.2006.02.001

Oefelein, J. C., & Sankaran, R. (2017). Large eddy simulation of reacting flow physics and combustion. In T. P. Straatsma, K. B. Antypas, & T. J. Williams (Eds.), *Exascale Scientific Applications* (1st ed., pp. 231–256). Chapman and Hall/CRC. https://doi.org/10.1201/b21930-11

Jarrin, N., Prosser, R., Uribe, J.-C., Benhamadouche, S., & Laurence, D. (2009). Reconstruction of turbulent fluctuations for hybrid RANS/LES simulations using a Synthetic-Eddy Method. *International Journal of Heat and Fluid Flow*, *30*(3), 435–442. https://doi.org/10.1016/j.ijheatfluidflow.2009.02.016

Task 3 - Thermoacoustic Modeling
Georgia Institute of Technology

Objectives
Lean pre-mixed combustors are susceptible to thermoacoustic instabilities, which increase emissions, decrease efficiency, reduce combustor life, and produce high-amplitude tonal noise. These instabilities occur in "islands" of the operating space that should be avoided during operation. Due to the wide range of potential operating conditions, it is not tractable to perform LESs or experiments across all relevant conditions to assess instabilities; instead, reduced-order modeling tools (i.e., thermoacoustic solvers) must be used. However, these tools have not been validated for the conditions and configurations of relevance for lean pre-mixed supersonic engine combustors. This task will develop, assess, and validate GE thermoacoustic solvers in this situation.

Research Approach
A layout of the geometry for the FTF measurements is shown in Figure 25, and a detailed description of the FTF measurements in the THOR rig can be found in Venkatesan *et al.* (2022). For compact flames with a flame length much shorter than the acoustic wavelength, the acoustic velocity at the flame base, the acoustic velocity at the same location and under the same operating condition but non-reacting, and the flame heat release oscillation are described as follows:

$$u'_{hot(1)} = u'_{cold(1)} + \bar{u}_1 \left(\frac{\bar{T}_{hot}}{\bar{T}_{cold}} - 1\right)\frac{Q'}{\bar{Q}} \quad (1)$$

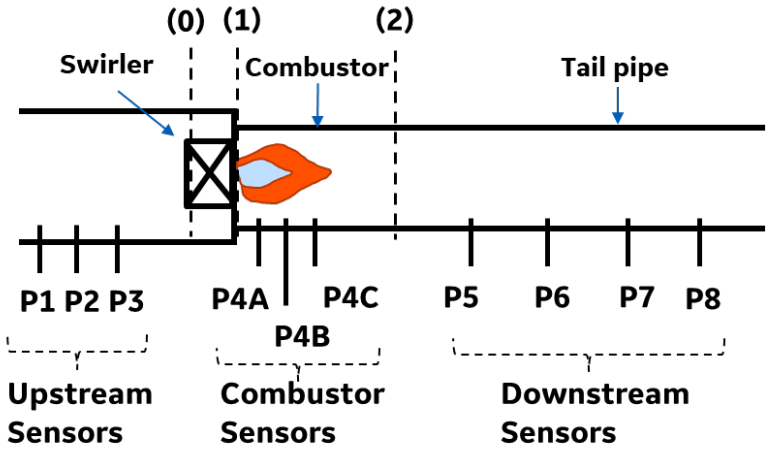

Figure 25. Illustration of the combustor, flame zone, and dynamic pressure sensors.

where $u'_{hot(1)}$ is the acoustic velocity at Location (1) for the reacting condition, $u'_{cold(1)}$ is the acoustic velocity at Location (1) for the non-reacting condition, $\overline{u_1}$ is the mean flow velocity at Location (1), Q' is the flame fluctuating heat release, ($\bar{Q}$) is the mean heat release, $\bar{T}_{hot}$ is the temperature in the combustor for the reacting condition, and $\bar{T}_{cold}$ is the temperature in the combustor for the non-reacting condition [2]. The FTF can then be written as follows:

$$FTF = \frac{\frac{Q'}{\bar{Q}}}{\frac{u'}{\bar{u}}} = \left(\frac{u'_{hot(1)}}{u'_{cold(1)}} - 1\right) / \left(\frac{\bar{T}_{hot}}{\bar{T}_{cold}} - 1\right) \quad (2)$$

During the measurements for a given operating condition, transfer functions between acoustic pressures at sensors P2–P8 with reference to P1 were obtained first for the non-reacting condition (also referred to as the cold or no-flame condition) and then for the reacting condition (also referred to as the hot or flame condition). The transfer functions were then processed to obtain acoustic velocities at the flame base, i.e., $u'_{cold(1)}$ and $u'_{hot(1)}$. Once the acoustic velocities are obtained, the FTF can be determined using Equation (2).

The air temperature in the tail pipe section is lower than the air temperature in the combustor for reacting conditions due to mixing with the window cooling flow and heat absorbed at the wall. To account for the effects of cooling air influx and non-uniform temperatures, two three-dimensional acoustic models were built using the finite-element solver COMSOL: one for the non-reacting condition and one for the reacting condition. The transfer matrix (TM) from the acoustic pressure and velocity at Location (2) to the acoustic pressure and velocity at Location (1) was then calculated using the acoustic models, with one TM calculated for the non-reacting condition and one TM for the reacting condition.

The measured acoustic pressure transfer functions from P5–P8 with reference to P1 were processed using the conventional multi-microphone technique (Polifke, 2001; Paschereit, 2002) to obtain the acoustic pressures and velocity at Location (2). The TMs were then used to determine the acoustic pressure and velocity at Location (1) as follows:

$$\begin{pmatrix} p' \\ u' \end{pmatrix}_1 = \begin{bmatrix} T_{11} & T_{12} \\ T_{21} & T_{22} \end{bmatrix} \begin{pmatrix} p' \\ u' \end{pmatrix}_2 \quad (3)$$

Once the acoustic velocities at Location (1) were obtained for both the non-reacting and reacting conditions, the FTF could be determined using Equation (2).

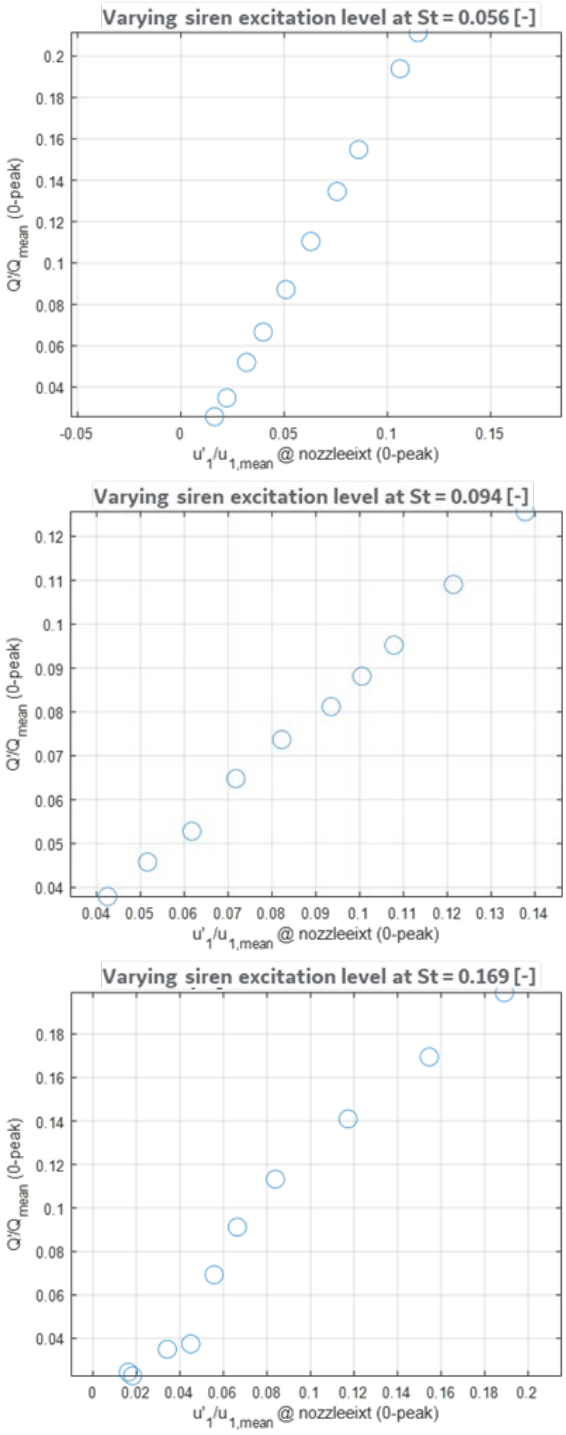

Figure 26. Linearity study at three Strouhal numbers. These frequencies spanned the full range of frequencies of interest.

Three pressure sensors (P1, P2, P3) were located upstream of the swirler. The inlet geometry upstream of the swirler can be considered uniform, as the cross-sectional area of the swirler was significantly smaller in comparison to the inlet plenum. The acoustic pressure and velocity immediately upstream of the swirler at Location (0) can be determined from the measured acoustic pressures at sensors P1–P3 using the conventional multi-microphone method. Combining the acoustic pressure and velocity at Location (0) and the acoustic pressure at Location (1), one can then obtain the swirler impedance as follows:

$$Z_{sw} = \frac{p'_{cold(0)} - p'_{cold(1)}}{u'_{cold(0)}\,\rho_{cold}\,c_{cold}\left(\frac{Area_{Comb}}{Area_{Swirler}}\right)} \tag{4}$$

where $p'_{cold(0)}$ and $u'_{cold(0)}$ are the acoustic pressure and velocity, respectively, immediately upstream of the swirler at Location (0), $p'_{cold(1)}$ is the acoustic pressure immediately downstream of the swirler at Location (1), and ρ_{cold} and c_{cold} are the mean air density and sound speed, respectively. Note that only acoustic pressures measured under non-reacting condition are needed to determine the swirler impedance. The acoustics of swirlers or burners are typically characterized by a TM that relates the acoustic pressure and velocity upstream of a swirler to the acoustic pressure and velocity downstream of the swirler (Paschereit, 2002). In this case, the axial dimension of the swirler is only approximately one tenth of the acoustic wavelength, even at 1000 Hz. Hence, the acoustic velocities upstream and downstream of the swirler were assumed to be equal, and the swirler could be characterized by the swirler impedance.

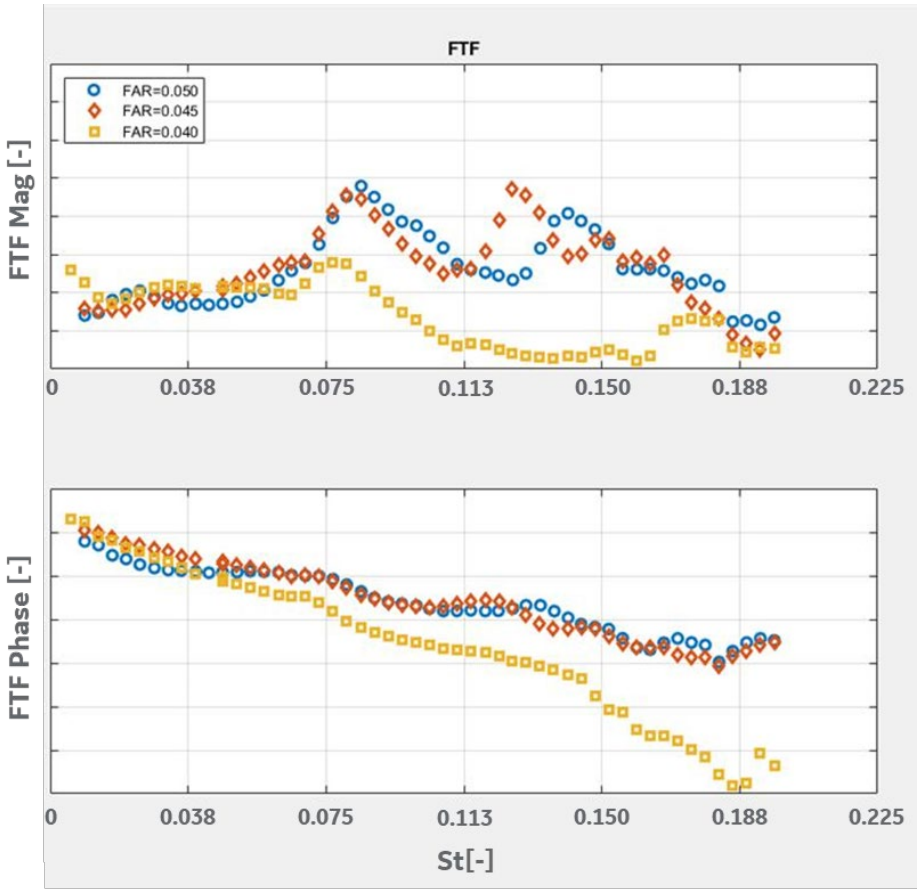

Figure 27. Acoustic flame transfer function (FTF) measurement for three different FARs.

It is well known that FTFs exhibit nonlinear behavior if the flame inlet air flow velocity perturbations become too large. In the current study, the FTFs were measured at different levels of inlet air perturbations to ascertain nonlinear behaviors. This linearity study was performed at a fixed combustor operating pressure, temperature, and equivalence ratio. The flame heat

release oscillation levels and the FTFs at the siren excitation frequency for $St = 0.056, 0.094,$ and 0.17 are shown in Figure 26 for varying levels of excitation.

In general, the flame heat release oscillation magnitude was observed to increase linearly with the flame base velocity excitation level. The deviation from linearity at very low excitation levels in Figure 26 is likely due to a higher background noise relative to the signal. However, the FTF magnitudes are observed to be linear at higher excitation levels. These results suggest that for the current measurements, the flame dynamics are in the linear regime and the FTFs obtained are linear.

Measurements of linear FTFs were undertaken for the range of operating conditions listed in Table 1. Specifically, the impact of the combustor inlet air temperature and thermal power on the FTF were each studied independently while the other operating parameters were held constant. Figure 27 shows the FTFs for three FARs (FAR1 > FAR2 > FAR3). The FTFs are observed to be strongly dependent on frequency and fuel-air ratio. The magnitudes of FTFs at the higher operating FAR are much higher across the entire frequency range, except for a narrow frequency band from $St = 0.028 - 0.056$. It is well known that liquid-fuel spray physics is highly dependent on the combustor operating FAR and temperature. High-speed CL images and flame videos of the combustor flame show changes in flame shape with changing FAR. The changes in flame shape and subsequent heat release are expected to impact the FTF response and will be the subject of detailed investigations and analyses moving forward.

Milestones

- ASCENT 74 test article designed for accurate FTF measurements
- Experimental Campaign 2 measurements of FTF performed

Major Accomplishments

- Acoustic and optical FTFs measured in the ASCENT 74 LPP combustor

Publications

Published conference proceedings

Venkatesan, K. (2022). Acoustic and Optical Flame Transfer Function Measurements in a High-Pressure Lean-Burn Aero-Engine Combustor Fueled with Jet A. ASME Turbo Expo.

Outreach Efforts

None.

Awards

None.

Student Involvement

- Mitchell Passarelli (PhD Candidate), GT: Mie scattering and OH* CL measurements
- Samuel Wonfor (PhD Candidate), GT: fuel PLIF measurements

Plans for Next Period

- Compare FTFs with analytical predictions and CFD
- Perform detailed comparisons of optical versus acoustic FTF methods

References

Venkatesan, K., Cross, A., & Han, F. (2022). Acoustic flame transfer function measurements in a liquid fueled high pressure aero-engine combustor. *Volume 3A: Combustion, Fuels, and Emissions*, V03AT04A049. https://doi.org/10.1115/GT2022-81769

Polifke, W., Paschereit, C. O., & Paschereit, K. (2001). Constructive and destructive interference of acoustic and entropy waves in a premixed combustor with a choked exit. *The International Journal of Acoustics and Vibration*, *6*(3). https://doi.org/10.20855/ijav.2001.6.382

Paschereit, C. O., Schuermans, B., Polifke, W., & Mattson, O. (2002). Measurement of transfer matrices and source terms of premixed flames. *Journal of Engineering for Gas Turbines and Power*, *124*(2), 239–247. https://doi.org/10.1115/1.1383255